EVALUATION OF TENSILE PROPERTIES FOR SELECTIVE LASER MELTED 316L STAINLESS STEEL AND THE INFLUENCE OF INHERENT PROCESS FEATURES ON STATIC PERFORMANCE

A Thesis

presented to

the Faculty of California Polytechnic State University,

San Luis Obispo

In Partial Fulfillment

of the Requirements for the Degree

Master of Science in Mechanical Engineering

by

Paul Swartz

June 2019

© 2019

Paul Swartz

ALL RIGHTS RESERVED

COMMITTEE MEMBERSHIP

TITLE:	Evaluation of Tensile Properties for Selective Laser Melted 316L Stainless Steel and the Influence of Inherent Process Features on Static Performance
AUTHOR:	Paul Swartz
DATE SUBMITTED:	June 2019
COMMITTEE CHAIR:	Thomas Mackin, Ph.D Professor of Mechanical Engineering
COMMITTEE MEMBER:	Xuan Wang, Ph.D Professor of Industrial and Manufacturing Engineering
COMMITTEE MEMBER:	Tom Mase, Ph.D Professor of Mechanical Engineering

ABSTRACT

Evaluation of Tensile Properties for Selective Laser Melted 316L Stainless Steel and the Influence of Inherent Process Features on Static Performance

Paul Swartz

Optimal print parameters for additively manufacturing 316L stainless steel using selective laser melting (SLM) at Cal Poly had previously been identified. In order to further support the viability of the current settings, tensile material characteristics were needed. Furthermore, reliable performance of the as-printed material had to be demonstrated. Any influence on the static performance of parts in the as-printed condition inherent to the SLM manufacturing process itself needed to be identified. Tensile testing was conducted to determine the properties of material in the as-printed condition. So as to have confidence in the experimental results, other investigations were also conducted to validate previous assumptions. Stereological relative density measurements showed that the as-printed material exhibited relative density in excess of 99%. Optical dimensional analysis found that the as-printed tensile specimens met ASTM E8 dimensional requirements in 14 out of 15 parts inspected. Baseline tensile tests indicated that the yield stress of the as-printed material is 24% higher than a cold-rolled alternative, while still achieving comparable ductility. The location of a tensile specimen on the build plate during the print was not found to have a significant effect on its mechanical properties. Theoretical behavior of notched tensile specimens based on finite element models matched experimental behavior in the actual specimens. Unique fracture behavior was found in both the unnotched reference and the most severe notch after microscopic inspection, and a root cause was proposed. Finally, extrapolating from previous studies and observing that experimental results matched theoretical models, it was determined that features inherent to SLM parts were not detrimental to the static performance of the as-printed material.

Keywords: additive manufacturing, AM, selective laser melting, SLM, 316L, as-printed, tensile

ACKNOWLEDGMENTS

This thesis was made possible by funding provided by Lawrence Livermore National Laboratory. Thanks to the various engineers at LLNL for creating unique opportunities for the students at Cal Poly.

I would like to thank the following individuals at Cal Poly for their various contributions along my academic journey:

Dr. Thomas Mackin, for inspiring enthusiasm for engineering throughout my six years at Cal Poly, starting in your dynamics class but especially over the past year.

Dr. Xuan Wang, for your support and technical insight over the years. You played an instrumental role in the success of both my senior project and now my thesis.

Dr. Tom Mase, for agreeing to support this thesis and providing unique insight.

Dr. Hans Mayer, for demanding the best from your students. You taught me to ask the hard questions and to take pride in my work.

John Fabijanic, for demonstrating that a healthy bit of skepticism is needed in life.

Dr. Russ Westphal, for helping me appreciate how cool engineering can be.

Hajime Yamanaka, for your patience and support in operating the SLM, the SEM, and the various metallography preparation equipment.

Dr. Trevor Harding and Dr. Blair London, for your willingness to lend me your time and resources, and for sharing your expertise in materials with me.

Anything I have ever achieved in my life was only possible because of the tremendous support that I have received from my family. I would like to thank my parents for all that they have done to raise me in an environment that allowed me to succeed. Hopefully one day I can fully comprehend the magnitude of your sacrifice. I would also like to thank my brother, Mike, for his constant presence throughout my various endeavors. Life's obstacles instantly become more manageable when we are laughing together.

TABLE OF CONTENTS

Page

LIST OF TABLES vii
LIST OF FIGURES viii
1. INTRODUCTION 1
1.1 Additive Manufacturing 1
1.1.1 Technology Overview 1
1.1.2 Powder Morphology 3
1.1.3 Advantages and Limitations 4
1.2 Objective 7
2. LITERATURE REVIEW 8
2.1 Powder Morphology 8
2.2 Research at Cal Poly 8
3. TESTING 10
3.1 Test Design 10
3.2 Test Procedure 13
4. RESULTS 15
4.1 Optical Microscopy 15
4.2 As-Printed Dimensional Accuracy 18
4.3 Tensile Test Data 22
4.3.1 Baseline Testing 22
4.3.2 Location Influence Testing 25
4.3.3 Notch Testing 28
4.4 FEA Results 33
4.4.1 Low Load Behavior 33
4.4.2 Global Yield Load Behavior 35
4.5 Fracture Behavior 37
4.5.1 Unnotched Failure 37
4.5.2 Notched Failure 39
4.5.3 Defect-Driven Failure 40
4.6 Further Investigation of Non-Defective Fractures 41
4.6.1 Mechanism for Ductile Pore Formation 41
4.6.2 Mechanism for Ductile Pore Distribution 44
5. CONCLUSION AND RECOMMENDATIONS 48
5.1 Conclusion 48
5.2 Recommendations 48
REFERENCES 50
APPENDICES
A. Engineering Drawings of Tensile Specimens 52
B. Dimensional Analysis Raw Data 59
C. Full Location Influence Testing Results 105

LIST OF TABLES

Table Page

1. SLM Settings 9

2. Notch Dimensions 12

3. Results of Relative Density Calculations 17

4. Optical Measurement Results 19

5. Summary of Tensile Test Results 24

6. Relative Differences in Material Properties 24

7. Summary of Results from Location Influence Testing 27

8. Global Yield Loads 32

9. Summary of ImageJ Porosity Analysis 45

LIST OF FIGURES

Figure Page

1. SLM Schematics. 3

2. SEM Photos of Powder Morphologies 4

3. Support Illustration 5

4 Support Material Photos 6

5. Residual Stress Mechanisms 7

6. Powder Measurements 8

7. Settings Iterations 9

8. Schematic of Subsize Tensile Specimen 10

9. As-Printed Tensile Specimens 11

10. Test Specimen Solid Models 13

11. Experimental Setup 14

12. Photo of a Density Cube with Side Length 10mm 16

13. Relative Density Images 17

14. Average Relative Density 18

15. Schematic of Optically Measured Dimensions 19

16. Optical Measurement Challenges 20

17. Geometry Calculated by the Micro-Vu Machine 20

18. Optical Dimensional Analysis Trends 21

19. Baseline Stress-Strain Trials 23

20. True and Engineering Stress-Strain Curves 23

21. 316L Property Map 25

22. Build Plate with Tensile Specimens Used for Location Influence Testing 26

23. Distribution of Yield Stresses across the Build Plate 27

24. Printing Error in Location Influence Samples 28

25. Load-Displacement Curves Using Crosshead Displacement 29

26. Experimental Setup for Notched Specimens 30

27. Stress-Strain Curves Created Using the Reduced Notch Area 31

28. Comparison of Baseline Dimension Stress-Strain Curves with Load-Displacement Curves for Notched Specimens 32

29. Annotated Load-Displacement Curves 33

30. Low Load FEA 34

31. Isometric section FEA 35

32. Global Yield Load FEA 35

33. Theoretical and Experimental Behaviors 37

34. Conclusion of a Baseline Tensile Test 38

35. SEM Images of a Fractured Baseline Specimen 39

36. Conclusions of Notched Tensile Tests 39

37. SEM Images of the Fracture Surface in a Notch 5 Specimen 40

38. Images of the Only Conclusively Defective Specimen 41

39. Ductile Fracture Structures 42

40. SEM Image of Oxide Pores 43

41. Strengths of HIP-ed 316L 44

42. Unnotched ImageJ analysis 44

43. Notch 5 ImageJ analysis 45

44. Scan Pattern Illustration 46

1. INTRODUCTION

1.1 Additive Manufacturing

1.1.1 Technology Overview

Additive manufacturing (commonly referred to as 3D printing) is a novel manufacturing method that has been growing for several decades. As opposed to subtractive manufacturing, which removes material from stock material to form the part geometry, additive manufacturing involves continuously adding constitutive material to itself in order to form the part geometry.

The process for making an engineering part with additive manufacturing is straightforward. Generally, a computer-aided design (CAD) file is created by an engineer, and a solid modeling program such as Solidworks or Creo is used to convert it from a CAD file to a stereolithography (STL) file. In this step, the part's smooth surfaces are divided into discrete triangles of a resolution defined by the engineer. Next, the STL file is opened in yet another software package that is used to define parameters specific to the particular 3D printing process. From there, depending on the process, the print job may be saved in yet another format to be imported by the printer, or may be sent to it directly.

There are several general types of additive manufacturing that can be applied to all kinds of materials [1]. Among the most popular are fused deposition modeling, stereolithography (SL), and various powder bed fusion (PBF) processes. Fused deposition modeling heats a polymer filament and extrudes it through a moving print head onto the build plate. SL uses UV-cure resin and a controlled UV light source to build a part on the build plate. PBF uses metallic powder and a laser to create a part on the build plate.

A popular type of PBF technology is selective laser melting (SLM), which uses a strong laser to provide enough heat to melt and fuse the powder together. The SLM125HL machine at Cal Poly (the SLM), made by SLM Solutions, uses this technology. Thus, the research conducted in this study should be regarded within the context of SLM additive manufacturing technology.

A common alternative to SLM is electron beam melting (EBM or e-beam). The main difference between e-beam and SLM is that the energy source is a powerful electron beam as opposed to a laser. Due to the high energy density of the e-beam, finer features can be produced than those made with SLM, and higher temperature alloys can be used.

A schematic of the SLM build chamber made by Sun, et. al [2] is shown below in Figure 1 next to a photo of the actual SLM125HL build chamber at Cal Poly. The available print area is defined by the size of the build plate and the maximum depth that it is designed to travel. Initially, the top surface of the build plate is level with the bottom surface of the build chamber. With each layer that is built, the build plate will descend by the defined layer thickness. The printing process begins when powder, enough for two layers' worth, is deposited from a large reservoir in the back of the machine, through a chute, and into the recoater. The recoater travels from one end of the chamber to the other, spreading powder along the build area with a rubber blade. After the powder has been spread, the fiber laser will trace the layer geometry on the powder, melting the particles together. Once the first pass is completed, the build plate will descend by one layer thickness and the recoater will return to its original position, depositing the remaining powder onto the build plate, followed by another pass of the laser. This process repeats until the complete part geometry has been created. At the beginning of the printing process, argon gas floods the build chamber while any existing air is evacuated. Then the argon is cycled continuously during the print to maintain the inert atmosphere. Overflow chutes allow extra powder to collect in receptacles placed beneath the build chamber. This powder can be recycled and used again in future prints.

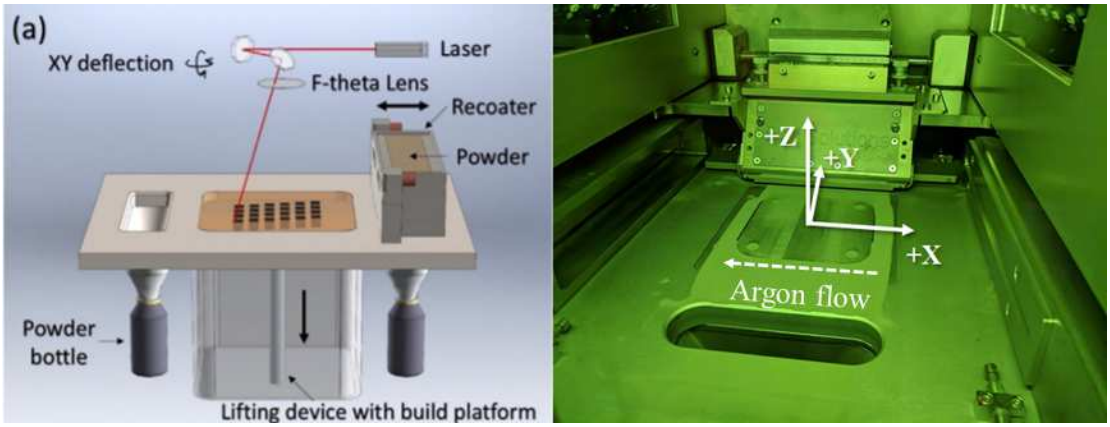

Figure 1. SLM Schematics. Left: selective laser melting build chamber, from Sun, et. al [2]. Right: Photo of the build chamber for Cal Poly's SLM125HL, with coordinate system added.

1.1.2 Powder Morphology

In any manufacturing process, it is important to consider the resulting product in the context of the initial material used. With SLM, the initial material is metallic powder. There are two main methods for manufacturing metallic powders: gas atomization and water atomization. Examples of both from work done by Li, et. al [3] are provided below in Figure 2. Gas atomized particles are more uniform in size and shape than those atomized by water. The material used with the SLM at Cal Poly is gas atomized 316L manufactured by LPW.

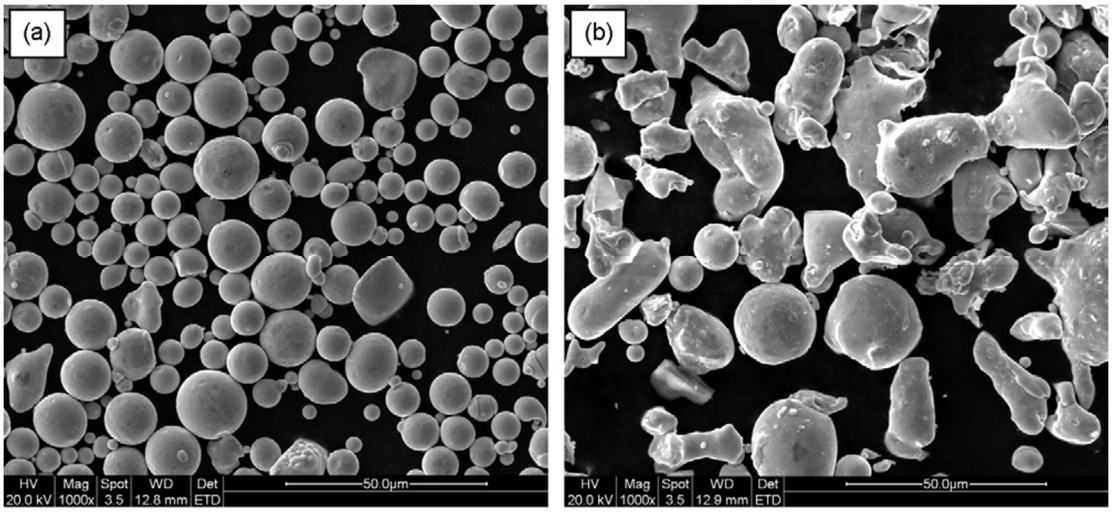

Figure 2. SEM Photos of Powder Morphologies. Left: gas atomized powder. Right: water atomized powder. Photos from Li, et. al [3].

1.1.3 Advantages and Limitations

Selective laser melting offers many opportunities that are not available using traditional manufacturing techniques. Complex part geometries are achievable due to the absence of any physical machine tools. Instead, the only tool interacting with the material is the laser beam. This also means that a production facility can create countless parts without needing to keep an inventory of specialty tooling. Furthermore, SLM has little consumable tooling, such as machining inserts, which can also pose significant financial challenges at production scale.

From a production standpoint, perhaps the most valuable benefit of SLM is the improvement in efficiency that it affords. It is possible for an operator to begin a print with several parts simultaneously on the same build plate, then continue working on other tasks while waiting for the print to finish. In order to produce the same quantity using traditional methods, the operator has to be present more often during the process. To magnify this benefit, a manufacturing facility might incorporate several SLM machines for still increased throughput.

When compared to alternative methods, SLM also offers reduced waste. Powder that is not used to form the finished product can be collected in overflow containers and sieved to separate agglomerated particles from usable ones. Powder that is small enough to pass through the sieving

machine is recycled for the next print. Only a small fraction of the powder left over from the print process is rendered non-recyclable. Reduced waste in manufacturing is less money spent per part, which translates to higher profits in production.

For all the advantages that SLM possesses, it is not without its limitations. Perhaps the most apparent of which is the need for use of support material. The central mechanism of SLM production is the layering of melted metallic powder to build a monolithic part. When the time comes for the laser to melt a new layer, powder that sits directly above the previous layer is rigidly supported by the substrate and layers can easily be built. Powder in an area where no prior layer exists is not rigidly supported by the part, but is only supported by the unmelted powder below it (see Figure 3 below). This presents issues in print quality on surfaces that overhang from the part below it. To combat this issue, the user can add structures that provide mechanical support for overhanging features.

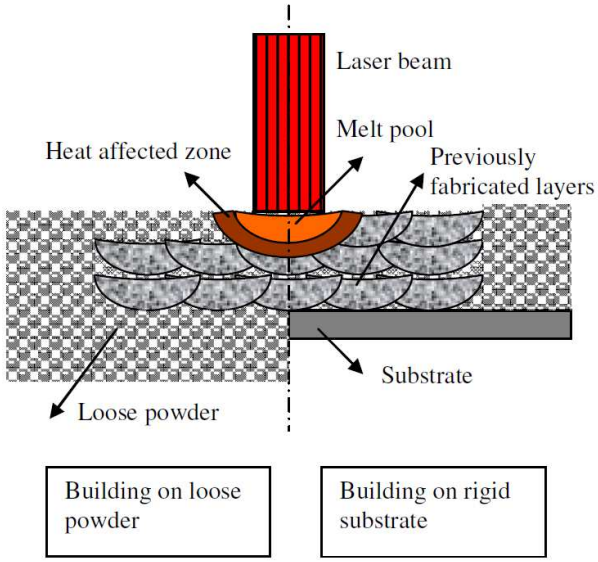

Figure 3. Support Illustration. Layers supported by loose powder are unstable, unlike those supported by a rigid substrate. Image from Kruth, et. al [4].

The challenge with adding support structures is identifying a method to remove it without affecting the main part in some way. In some cases, as with support material used only to offset

parts from the build plate, the solution is relatively simple: parts are removed from the build plate using a band saw, and the remaining support material is sanded off the bottom of the part. Depending on the resources available, wire electrical discharge machining (EDM) can also be used to provide a more elegant alternative to a band saw cut. In other cases, the solution is not as straightforward. Photos of different support material applications appear below in Figure 4.

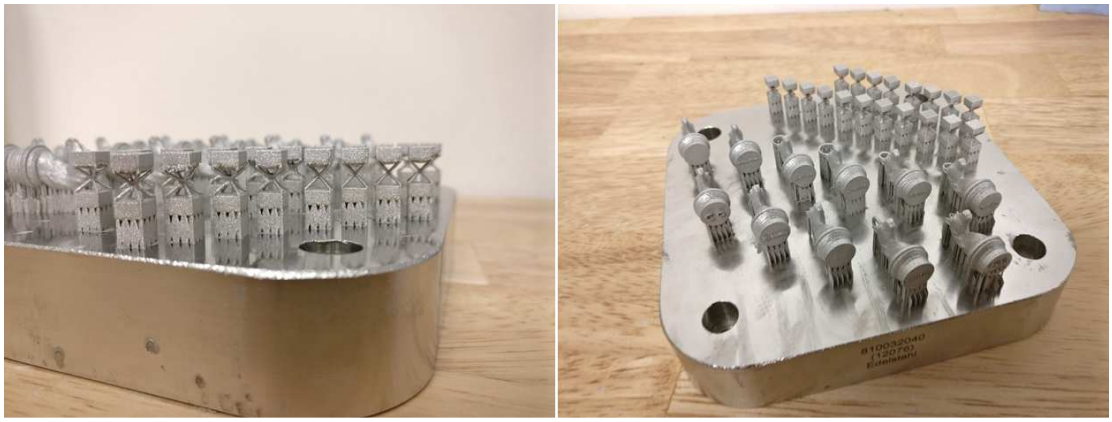

Figure 4. Support Material Photos. Left: Lattice unit cells where support material is used only to offset the bottom plane of the part from the build plate, and is removed relatively easily. Right: Chess pieces where support material removal is not straightforward and requires more attention. Photos courtesy of Julia Rios, Cal Poly.

Another complication of SLM is the presence of residual stresses. Residual stresses arise from the thermal effects related to the cyclic heating and cooling of the topmost layers of powder during each pass of the laser. Kruth, et. al [5] showed that the mechanism for residual stress development is the plastic compression (aided by decreased yield stress at high temperature) of the material directly adjacent to the laser during heating. Upon cooling, recently heated layers will begin to shrink. Unconstrained, the plastically compressed (and consequently, shorter) layers would cause the upper surface of the part to deflect in a convex manner in order to reconcile the size discrepancy. However, since the material is fully constrained to the bottom of the build plate, it is unable to warp, thus creating the residual stress state in as-printed parts. Figure 5 below illustrates this mechanism and its effect on the final geometry of a part.

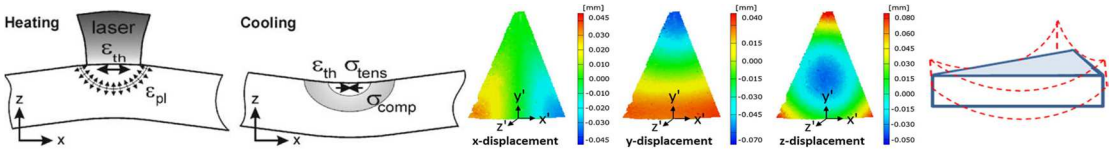

Figure 5. Residual Stress Mechanisms. Left: Schematic illustrating material responses to heating and cooling during SLM, from Kruth, et. al [5]. Right: Experimental results of Wu, et. al [6], showing warpage induced by residual stresses created during SLM.

1.2 Objective

Previous work was conducted to begin optimizing print parameters for the SLM125HL machine at Cal Poly. This was a crucial step toward producing SLM parts with consistent build quality, as preliminary investigation suggested that the material properties of parts in the as-printed condition might be comparable to commercially available 316L material. In order to further support the viability of the current SLM settings, tensile material characteristics are needed. Furthermore, it must be demonstrated that the performance of the as-printed material is reliable. Having these results on hand will be useful when designing SLM parts for future research and engineering applications. Finally, any influence on the static performance of parts in the as-printed condition inherent to SLM manufacturing must be identified.

2. LITERATURE REVIEW

2.1 Powder Morphology

Kamath, et. al [7] performed a powder morphology study for the material used in their study, which happened to include 316L powder from LPW. Their characterization is presented below in Figure 6. Note that the distributions are centered about 30-40µm and 50µm when measuring distribution by diameter and volume, respectively. This discrepancy would suggest that the powder is not uniformly spherical. For the purposes of this research, the morphology of the powder used will be assumed to exhibit similar distributions.

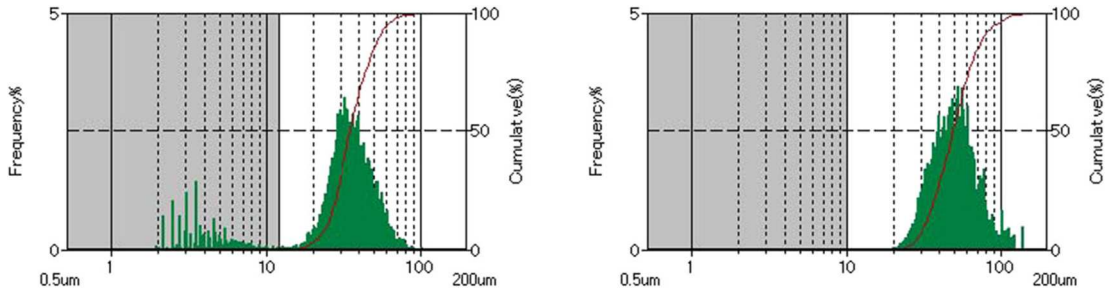

Figure 6. Powder Measurements. Measured size distributions of 316L powder manufactured by LPW, from Kamath, et. al [7]. Left: Distribution based on measured diameter. Right: Distribution based on measured volume.

2.2 Research at Cal Poly

Much research has been done at Cal Poly since the installation of the SLM125HL machine, including a number of undergraduate senior projects and master's theses. None have been more impactful than the work done by Sebastian Pohl [8] to identify optimal machine parameters for print quality optimization.

The central experiment in Pohl's work involved printing several 316L cubes arranged in a matrix. On one axis of the matrix, laser power (in Watts) was varied linearly, and on the other axis, scanning speed (in mm/s) was also varied linearly. Combined, a wide design space of linear energy density terms (in J/mm) were sampled and the results inspected. With each iteration of the

experiment, the range of sampled energy densities was refined based on the results from the previous test. In total, three trials were conducted (pictured below in Figure 7). After the third trial was completed, an optimal combination of laser power and scan speed was determined by evaluating relative density, hardness, surface roughness, and visual inspection.

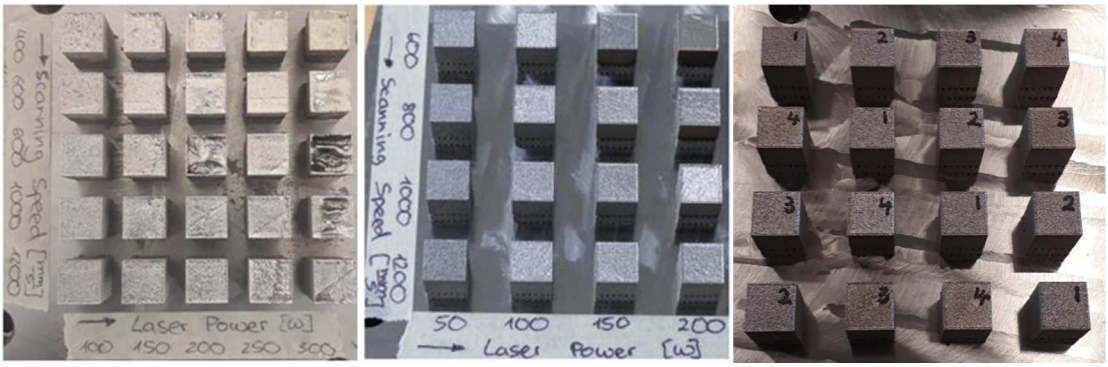

Figure 7. Settings Iterations. Photos from Pohl's [8] SLM parameter optimization trials at Cal Poly. Input settings were refined between the first trial (left), and the final trial (right).

The optimal settings, as determined by Pohl, are 150W laser power and 1000mm/s scanning speed. All other settings in those trials were held constant, including the 70µm laser spot size, so it is worth noting that print quality could potentially be improved further by refining more settings. For the purposes of the research presented in this thesis, all settings were left unchanged from Pohl's work, which are listed below in Table 1.

Table 1. SLM Settings. Optimal settings for the SLM125HL at Cal Poly, taken directly from Pohl [8].

Build Order: Inside to Outside			
Hatch → Contour → Border			
Layer Thickness			30 µm
Hatching Distance			120 µm
Inskin Scanning	Borders	Power	75 W
		Speed	312.5 mm/s
	Fill Contours	Power	112.5 W
		Speed	562.5 mm/s
	Hatches	**Power**	**150 W**
		Speed	**1000 mm/s**

3. TESTING

3.1 Test Design

When it comes to characterizing the mechanical properties of a material, one of the most useful methods is arguably also the most fundamental: the tensile test. The procedure involves placing a test coupon in a machine that pulls on the material until the test is completed, which is usually when the test coupon fractures. The machine records time, load, and displacement data, which can be used to create an engineering stress-strain curve, given the geometry of the test coupon.

All baseline tensile testing in this research was conducted within the specification of ASTM E8, *Standard Test Methods for Tension Testing of Metallic Materials* [9]. Figure 8 below shows the geometry of the subsize plate-type tensile specimen used. The complete drawing is also included in Appendix A.

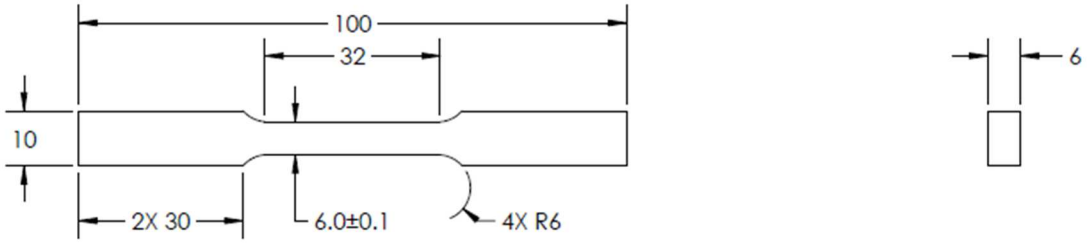

Figure 8. Schematic of Subsize Tensile Specimen. All dimensions are in millimeters and follow ASTM E8 specification [9]. The complete drawing is included in Appendix A.

Liverani, et. al [10] demonstrated that there are differences in tensile test results related to the build orientation of the test coupons. There are two main challenges with printing parts with large dimensions in the XY-plane, such as tensile bars printed in a flat, horizontal orientation, or at 45° from vertical. The first is that there is more support material required to build these parts. More support material used also means that more support material must be removed, and it can be difficult to remove support material completely without affecting the geometry or mechanical properties of the final part. Second, Wu, et. al [6] found that layers with large melt pools create

residual stresses in AM parts, which will result in warpage upon removal from the build plate. Therefore, in order to minimize both support material removal and residual stresses, tensile bars were arranged so that they would be printed vertically, in the Z-direction (see Figure 9 below).

Figure 9. As-Printed Tensile Specimens. Printing in the Z-direction minimizes the amount of support material required.

Further testing beyond baseline tensile trials was needed to observe whether the SLM process affected the ductility of as-printed parts. One way to do this is by conducting notched tensile tests to observe the static notch sensitivity. Introducing a stress concentration will lower the load at which an otherwise unchanged tensile bar will fail. If the failure in the notched section is ductile, then it can be concluded that there is not any mechanism inherent to the SLM process that affects ductility. However, if the notched failure is brittle, then it could be possible that some feature of SLM parts, such as porosity or the surface condition, contributes to adverse failure characteristics. Therefore, baseline ASTM E8 tensile specimens are modified to include notches of various sizes. Several notches are needed so that, in the event of brittle failure, a ductility limit may be identified for design.

Notches are commonly introduced to parts via machining, as is common with dynamic testing, in order to control the precision of the notch geometry and the sharpness of the root radius

where a crack is likely to begin. In the case of this research, the purpose was to observe the static notch sensitivity for a geometry more closely resembling a stress concentration that might realistically appear in design. Thus, the notches used for testing needed to be printed into the test specimens.

In addition to selecting a notch geometry representing a realistic stress concentration factor, the notch's viability for 3D printing needed to be considered. After surveying different types of notch geometry, shallow, double-edged notches were selected. Based on the 40° critical self-supporting angle determined by Pohl, this notch geometry lends itself to unsupported printing in the Z-direction. Dimensions for five notch geometries are provided below in Table 2 and illustrated in Figure 10. Note that the root radius, the radius of the notch, is constant. The reduced width is defined as the width of the specimen at the root of the notch.

Table 2. Notch Dimensions. Specimen 0 is the unnotched baseline from ASTM E8 [9].

Specimen/ Notch No.	Root Radius [mm]	Reduced Width [mm]
0	2.5	6.0
1	2.5	5.5
2	2.5	5.0
3	2.5	4.5
4	2.5	4.0
5	2.5	3.5

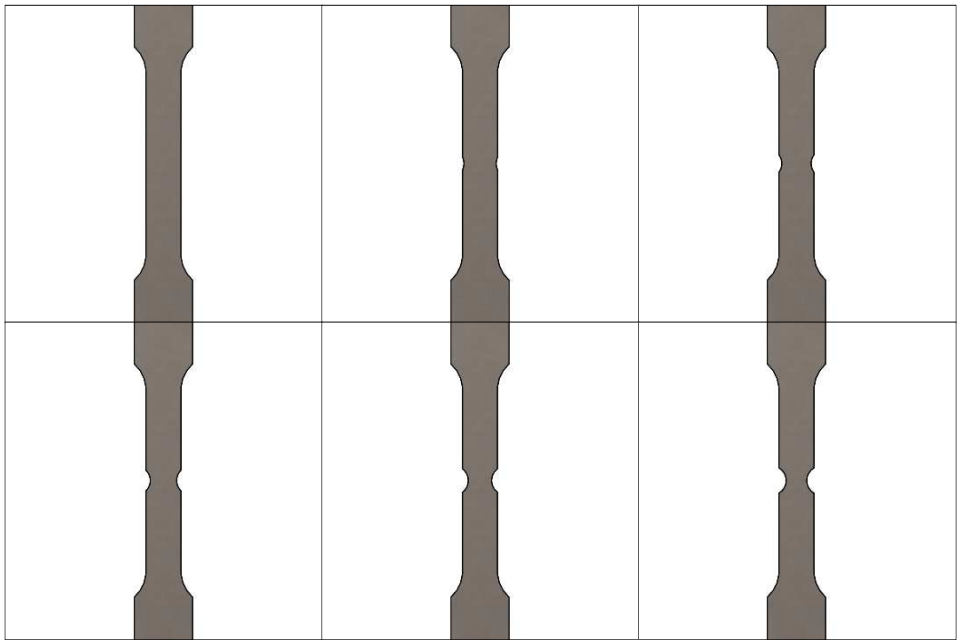

Figure 10. Test Specimen Solid Models. Solid models of tensile specimens created with Solidworks. Top row: Specimens 0-2. Bottom row: Specimens 3-5.

3.2 Test Procedure

Tensile testing was performed according to ASTM E8 specification with the help of Cal Poly's Materials Engineering Department. The machine used for all trials was an Instron model 5584 equipped with a 150kN load cell and flat grips. During the elastic portion of a test trial, strain was applied at a rate of 3mm/min and measured using an Epsilon model 3542-012M-010-ST extensometer. Once the trial eclipsed 1.5% strain, the strain rate was programmed to automatically change to 8mm/min. The test concluded when the measured stress dropped by more than 40%, indicating the fracture of the test specimen. Figure 11 below shows the experimental setup prior to commencing a test.

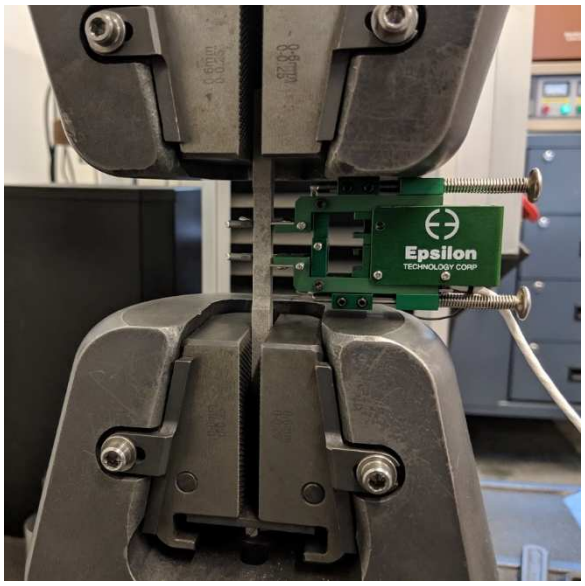

Figure 11. Experimental Setup. An Instron model 5584 was equipped with flat grips and an Epsilon extensometer was used to record elastic strain.

4. RESULTS

4.1 Optical Microscopy

In order to evaluate the viability of SLM tensile bars, the process parameters employed must first demonstrate the capability to produce near-full density parts. Pohl [8] performed rudimentary relative density measurements, using a micrometer to measure dimensions and a scale to measure weight, en route to identifying ideal print settings. He notes, however, that his determination of processing parameters was based on the relative maximum value for measured relative density, since his measurement technique was not appropriate for quantitative density evaluation, given the surface roughness of the parts. Spierings, et. al [11] investigated several techniques for determining the relative density of SLM parts, and found that, at low porosities, microscopy can yield results similar to the Archimedes method approach outlined by ASTM B311-17, *Standard Test Method for Density of Powder Metallurgy (PM) Materials Containing Less Than Two Percent Porosity* [12]. In the absence of the equipment necessary for conducting the Archimedes procedure, microscopy analysis was conducted using resources readily available through Cal Poly's Materials Engineering department.

A single cube of side length 10mm, shown in Figure 12, was printed in the center of the build plate using the settings determined by Pohl. Following the recommendation of Spierings, et. al [11], the cube was sectioned vertically, mounted, and polished to a 0.5µm finish.

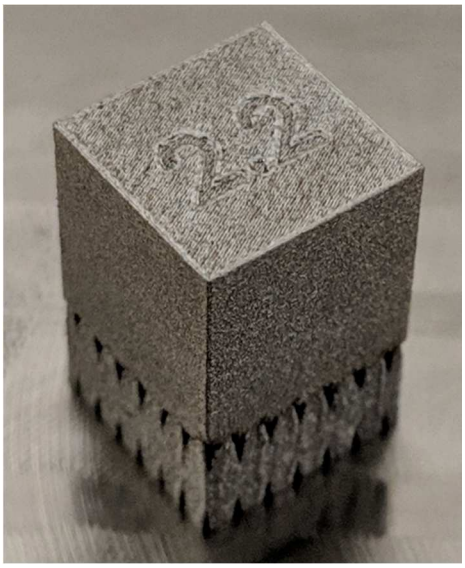

Figure 12. Photo of a Density Cube with Side Length 10mm. As-printed density cube shown.

After polishing, the section was examined using an Olympus BX41 microscope. Photographs were taken at 50x magnification at multiple locations across the surface of the polished section. Then, using ImageJ, a free software program developed by the National Institutes of Health, these photos were converted to binary black and white images, where the black regions are the pores. Using these images, shown below in Figure 13 along with the original photos, ImageJ was able to determine the area fraction of pores in the image. This value is interpreted to reflect the porosity of the image, and relative density of the image is obtained by subtracting this value from 100%. Calculated values for the relative density of each image are listed below in Table 3. Note that the contrast settings for images 1 and 5 were set manually because ImageJ was unable to automatically convert the photos with the default black and white settings. Thus, it is likely that the area fraction of porosity calculated by ImageJ for these images is slightly affected.

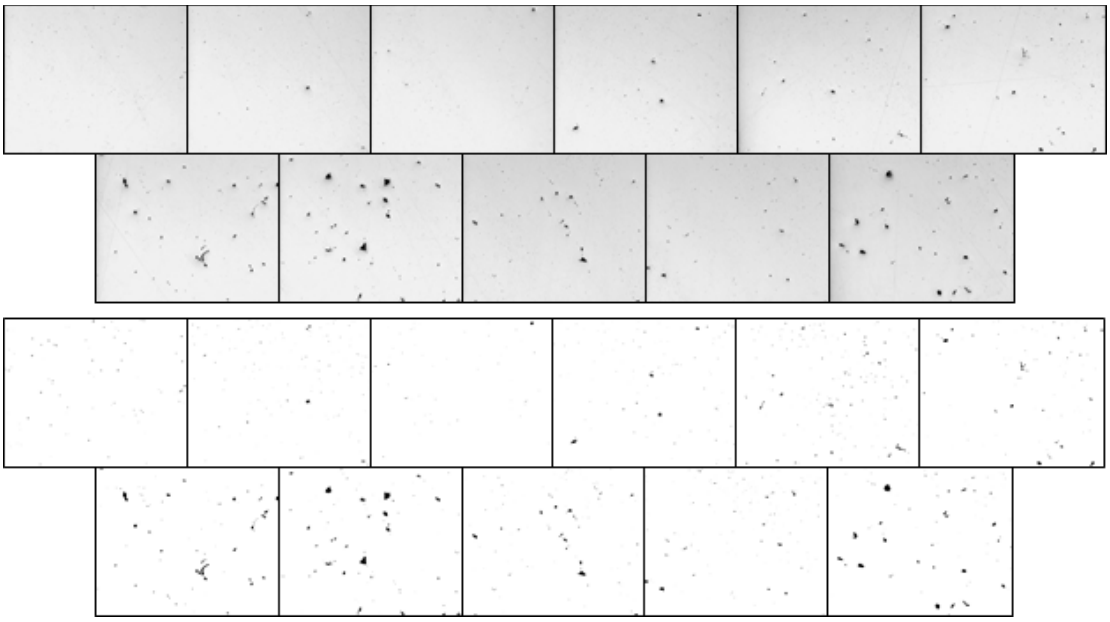

Figure 13. Relative Density Images. Images show how ImageJ was used to determine relative density. Top two rows: original microscope photos, taken at 50x magnification. Bottom two rows: Results of ImageJ processing.

Table 3. Results of Relative Density Calculations. Area fraction values are left exactly as calculated by ImageJ and subtracted from 100% to obtain relative densities. Binary thresholds for images 1 and 5 were determined manually.

Image No.	Area Fraction [%]	Relative Density [%]	Image No.	Area Fraction [%]	Relative Density [%]
1	*0.124*	*99.876*	7	0.592	99.408
2	0.153	99.847	8	0.815	99.185
3	0.059	99.941	9	0.363	99.637
4	0.186	99.814	10	0.249	99.751
5	*0.355*	*99.645*	11	0.684	99.316
6	0.319	99.681			

The mean relative density value obtained from these images was 99.6%, with a standard deviation of 0.24%. A photo with 99.6% relative density and the corresponding binary image are displayed in Figure 14. If it is assumed that the relative density of the cross section is stereologically equivalent to that of the whole part, then the build parameters specified by Pohl are able to consistently produce parts in excess of 99% relative density.

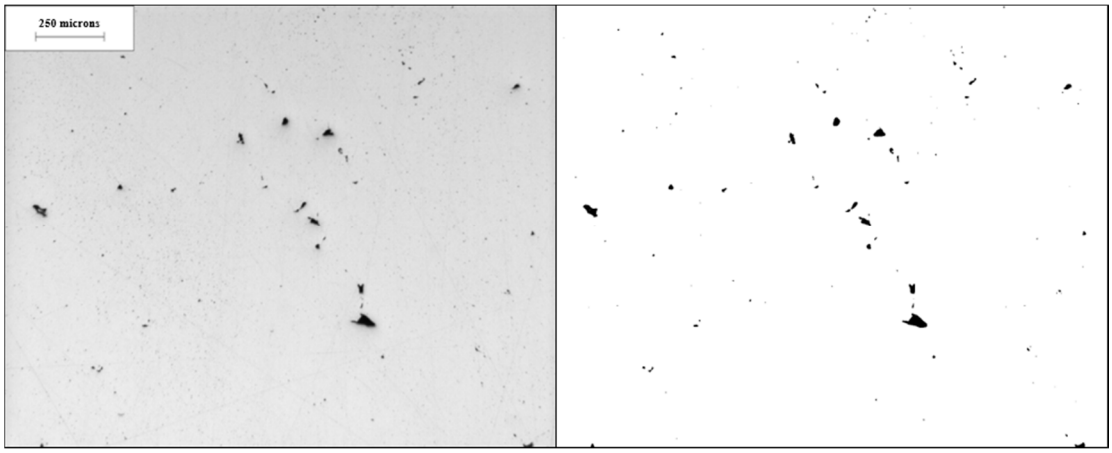

Figure 14. Average Relative Density. Left: Microscope image no. 9, which had a relative density of 99.6%. Right: ImageJ binary conversion provided for reference.

Pohl's parameter optimization findings have been used in conjunction with both striped and chess board/island scan patterns. Although the density measurements discussed were conducted using a stripe pattern, Kamath, et. al [7] demonstrated that an island pattern is capable of producing similar results. Wu, et. al [6] found that parts printed flat (i.e. major axis in the XY-plane) are susceptible to residual stress-induced deflection upon removal from the build plate, and that using a small island scan pattern helps mitigate this issue. Since all tensile bars in this research were printed with the major axis in the vertical (Z) direction, residual stress effects are assumed to be negligible. Therefore, it is assumed that the results presented in this research are not affected by the scan pattern selected.

4.2 As-Printed Dimensional Accuracy

Pohl [8] demonstrated that when SLM parameters are not optimized, the resulting geometry is severely affected. What had not been demonstrated, however, was the accuracy to which dimensional tolerances are achievable with the tuned print settings. An investigation into the print accuracy of SLM parts was conducted for this research in the interest of meeting ASTM E8 requirements. Using a Micro-Vu VERTEX 312UC optical measuring machine, 15 unnotched tensile bars were inspected for their dimensional accuracy according to ASTM E8 specification for

subsize specimens. The results of the dimensional inspection are summarized below in Figure 15 and Table 4. Complete results generated by the Micro-Vu machine are also included for reference in Appendix B.

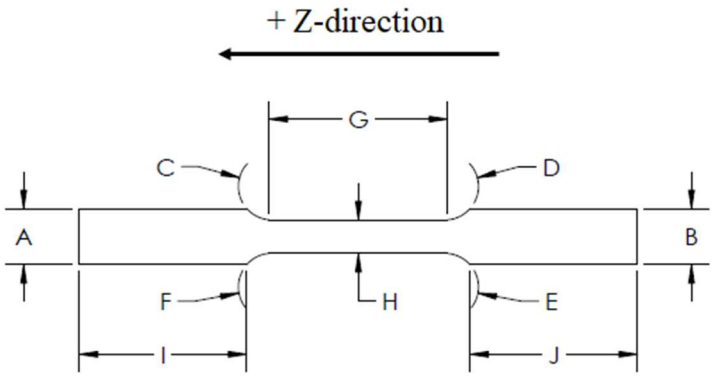

Figure 15. Schematic of Optically Measured Dimensions.
Flatness K and Distance L, the part thickness, are not shown.

Table 4. Optical Measurement Results. Note that there is no nominal flatness callout.

Type	Letter	Nominal [mm]	Average Difference [mm]	Standard Deviation [mm]	Coefficient of Variation [%]
Distance	A	10	0.0666	0.0216	0.9%
Distance	B	10	0.0798	0.0296	1.1%
Radius	C	6	-0.1364	0.3634	3.8%
Radius	D	6	-0.0828	0.1737	1.5%
Radius	E	6	-0.0905	0.2961	3.4%
Radius	F	6	-0.1972	0.2546	1.0%
Distance	G	32	-0.1732	0.1874	0.0%
Distance	H	6	0.0633	0.0213	1.4%
Distance	I	30	0.0789	0.0370	0.4%
Distance	J	30	0.3040	0.0396	1.1%
Flatness	K		0.2909	0.0162	
Distance	L	6	0.0368	0.0176	0.9%

These results indicate the SLM's ability to consistently achieve most straight features within 0.1mm. The standard deviations for most of these features were within 0.040mm, or 40µm, which is on the order of a single particle diameter. The largest deficiency of the SLM is its inability to produce continuously changing geometries in the Z-direction, such as shoulder radii. In the case of tensile bars, all four radii are undersized, with the standard deviation reaching up to 0.36mm, or

a coefficient of variation of 6.1% for a nominal value of 6mm. Furthermore, straight features dependent upon the accuracy of the shoulder radii, such as Distance G, the gauge length, are also affected. Several times, the Micro-Vu machine was unable to determine the intersection point of the radius and the gauge length edges, illustrated in Figure 16, which was a crucial feature for defining Distance G.

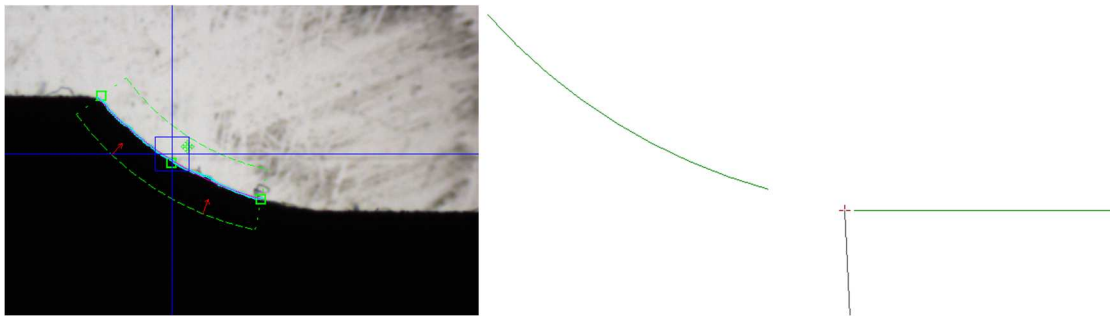

Figure 16. Optical Measurement Challenges. Example of an instance in which the Micro-Vu machine was unable to determine the intersection of the shoulder radius and the gauge length. Left: Camera view. Right: Calculated geometry.

Since the program was occasionally unable to detect the actual intersection, the points used to calculate Distance G, illustrated by the dashed line in Figure 17, had to be located manually apart from the automated program. Thus, the standard deviation of Distance G, the gauge length, was nearly 0.2mm.

Figure 17. Geometry Calculated by the Micro-Vu Machine. Note that the gauge length, shown by the dashed line, must be calculated indirectly.

Another area of interest in this investigation, while not crucial to determining the tensile properties, was the flatness of the tensile bars made with the SLM. Measured by averaging the

maximum differences in contrast of various locations across one XZ face of each specimen, the average flatness of the tensile bars was 0.2909mm, and the standard deviation was 0.0162mm, or 16.2µm. Given that Kamath, et. al [7] found that the powder particle size can vary widely up to 50µm in diameter, the resulting surface flatness is surprisingly consistent.

Figure 18 summarizes the trends observed from the dimensional analysis. Each data point represents one of the dimensions listed in Table 4. The closer a dimension is to the middle of the graph, the closer, on average, it is to its nominal value. Data that is closer to the bottom of the graph has a lower standard deviation, and therefore the dimension is achieved more consistently. The SLM is able to consistently generate straight features that are somewhat oversized, with the average differences and standard deviations both on the order of one or two particle diameters.

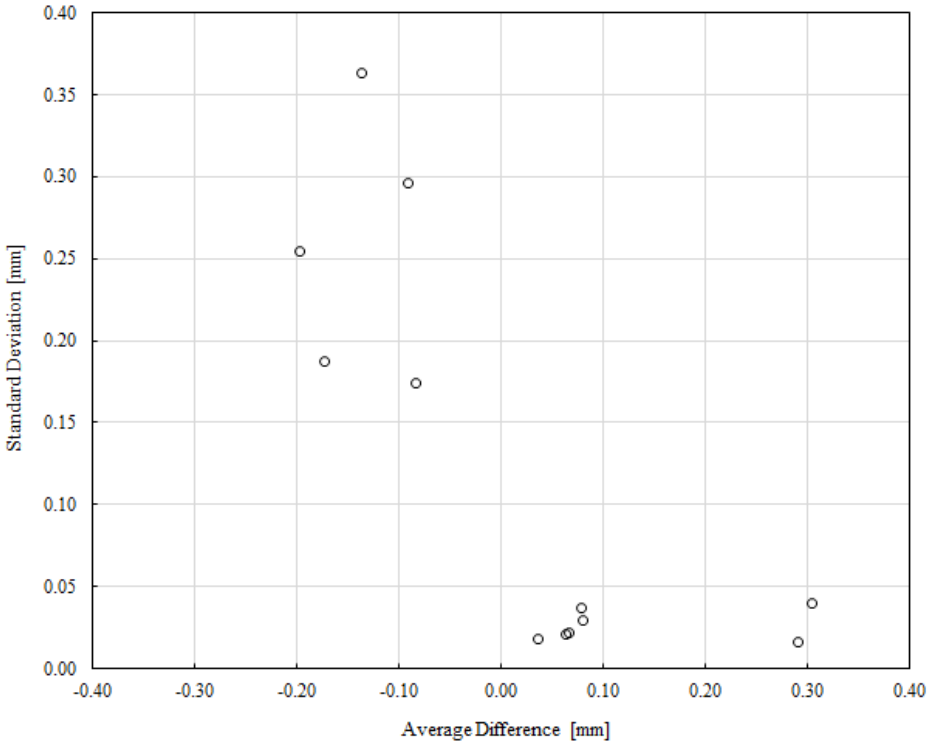

Figure 18. Optical Dimensional Analysis Trends. Straight features are generally more easily achievable than round ones.

The dimensions that are most oversized are Distance J and Flatness K. Distance J is understandably oversized as a result of the manual sanding process employed to remove the support

material that attached the bottom of the samples to the build plate. There is no specification in ASTM E8 for specimen flatness, so the measurements of Flatness K were taken only in hopes of gaining further insight into the quality of SLM parts.

All four radii were undersized and exhibited variability on an order well above several particle diameters. As a result, Distance G also exhibited undersized behavior with wide variability. Per ASTM E8, the only dimension with a critical tolerance is the section width (Distance H in Table 4), which is to be within ±0.1mm. Fortunately, the SLM is able to meet this requirement with a standard deviation of 0.0176mm, or 17.6μm. Of the 15 samples inspected, only one did not meet this requirement.

4.3 Tensile Test Data

4.3.1 Baseline Testing

Plots of tensile responses for seven samples are shown in Figure 19. An average engineering stress-strain curve was composed from those seven trials, from which the true stress-strain curve was obtained using equations (1) and (2). Both curves are presented in Figure 20, while the average tensile properties useful for design that arose from those seven trials are also presented alongside reference values summarized in Table 5.

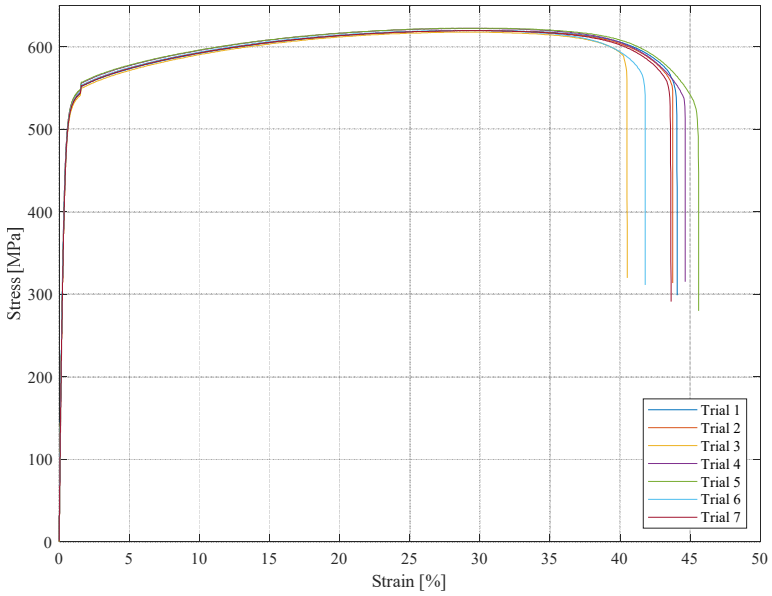

Figure 19. Baseline Stress-Strain Trials. Data from all trials exhibited consistent strength and ductility.

$$\varepsilon_T = \ln(1 + \varepsilon) \tag{1}$$

$$\sigma_T = \sigma \cdot e^{\varepsilon_T} \tag{2}$$

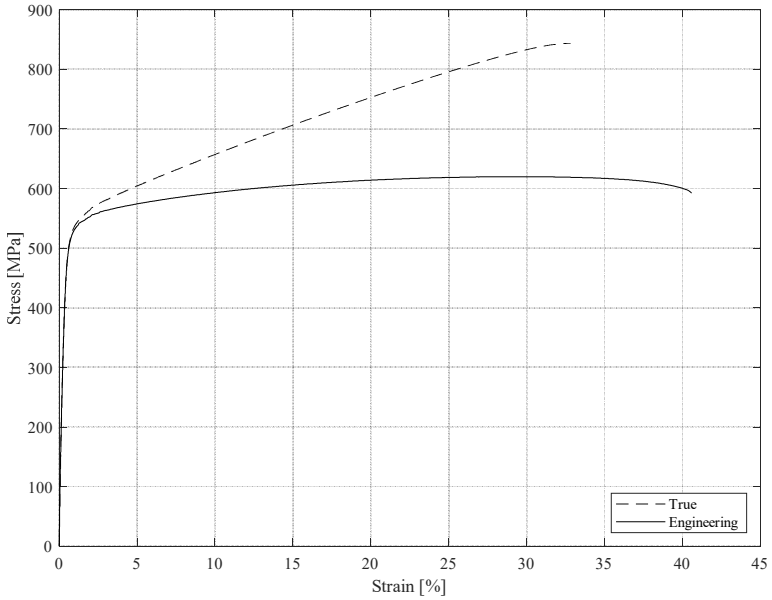

Figure 20. True and Engineering Stress-Strain Curves. Average curves were derived from the seven baseline trials.

Table 5. Summary of Tensile Test Results. Values of comparable alternative materials are provided for reference.

		Young's Modulus [GPa]	Yield Stress [MPa]	Tensile Stress [MPa]	Elongation [%]
SLM	Average	170	470	620	43
	Standard Deviation	10	6.8	1.7	1.7
	Coefficient of Variation [%]	5.9	1.5	0.28	4.0
Annealed 316L Bar [13]		193	205	515	60
Cold Drawn 316L Bar [14]		193	380	585	45

Baseline results for tensile tests proved to be promising. A summary of relative differences from the published data are listed in Table 6. For cold drawn 316L bar [14], as-printed SLM material shows a 24% increase in yield stress while maintaining comparable elongation.

Table 6. Relative Differences in Material Properties. Values represent the difference of the as-printed SLM material from commercially available alternatives.

Reference Material	Young's Modulus	Yield Stress	Tensile Stress	Elongation
Annealed 316L Bar [13]	-12%	+130%	+20%	-28%
Cold Drawn 316L Bar [14]		+24%	+6.0%	-3.5%

The properties of the as-printed material were compared to an existing survey of achievable 316L properties presented in the work published by Wang, et. al [15] in Figure 21. The graph includes conventional properties as well as those achieved with other powder bed fusion techniques. Note that the “Our work” annotation refers to the work conducted by the original authors, whereas the results of this study are represented by the hexagon and dashed lines.

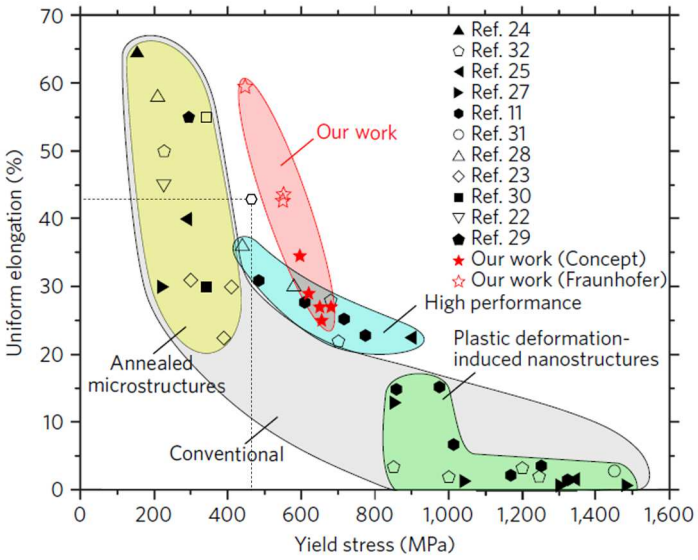

Figure 21. 316L Property Map. Tensile properties achieved by various conventional and PBF techniques [15], superimposed with results observed in this study.

4.3.2 Location Influence Testing

Further testing was performed to investigate whether the tensile properties are skewed by the specimen's location on the build plate, and/or if printing several parts simultaneously in close proximity would affect the experimental results. A photo of the build plate configuration used is shown in Figure 22.

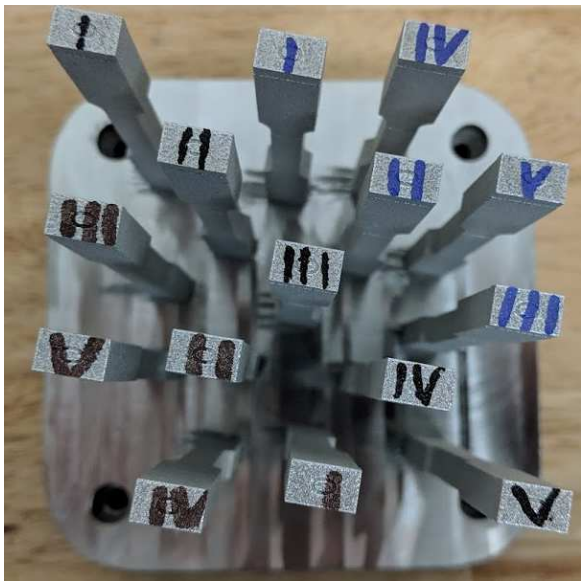

Figure 22. Build Plate with Tensile Specimens Used for Location Influence Testing.

Fitzgerald and Everhart [16] found that “an effect of the spacing between parts in a build had an effect on tensile properties if the spacing was large enough, but below 40 mm there was no significant difference in performance.” This finding is confirmed by the results shown below in Figure 23, which illustrates the distribution of yield stresses for 15 tensile bars. There is a slight trend along the X-axis, but the total range of values is within 5% of the average. Fitzgerald and Everhart also observed this trend, and suggested that the argon gas flowing from positive to negative X could create nonuniform convection and thus play a minor role in the resulting distribution of yield stresses.

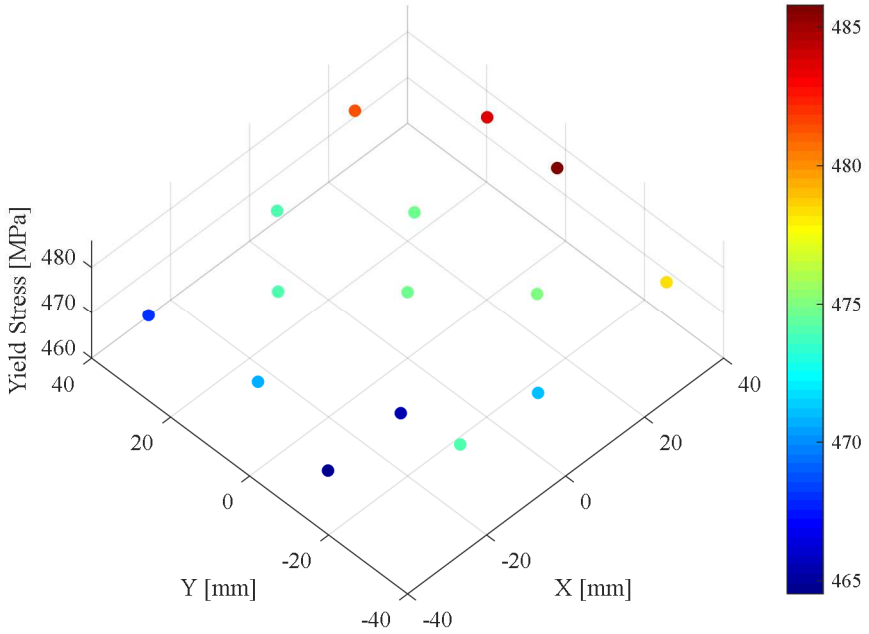

Figure 23. Distribution of Yield Stresses across the Build Plate. Note that the total range of values spans less than 5% of the average.

A summary of the results is presented in Table 7, and full results are provided in Appendix C. Data for Young's modulus and yield stress are remarkably similar to the previous baseline data.

Table 7. Summary of Results from Location Influence Testing. While plastic data was widely variable due to a printing fault, the elastic results are similar to previous baseline data.

	Young's Modulus [GPa]	Yield Stress [MPa]	Tensile Stress [MPa]	Elongation [%]
Average	170	470	590	23
Standard Deviation	11	6.1	32	16
Coefficient of Variation [%]	6.5	1.3	5.5	70

Results for tensile stress and elongation were negatively affected by a manufacturing error when the SLM ran out of 316L powder, pausing the print overnight. The consequence of this interruption was that the samples fractured at the exact location where the print had stopped, producing a wide variation in measured tensile stresses and elongations. Upon closer inspection, it

was observed that after resuming the print, the remaining part geometry continued building at a slight offset from the previous geometry. Photos of both the fracture and the offset are displayed in Figure 24. The sharp geometric discontinuity, which generates a stress concentration, as well as any local metallurgical changes, must have been what made the plastic data for these trials unusable. However, based on the agreement of the elastic data and the consistency of the plastic results for the baseline trials in Figure 19, it is reasonable to assume that the plastic data would likely have also been similar to the previous baseline.

Figure 24. Printing Error in Location Influence Samples. Left: A failed specimen after tensile testing. Right: The root cause of the failure was a subtle offset between the geometries printed before and after the machine paused.

4.3.3 Notch Testing

Once the baseline was established and verified, the next phase of tensile testing involved specimens with various notches printed in the middle of the gauge length. These tests posed a unique challenge: determining a method to accurately evaluate the stress-strain behavior in the notch, where the distributions of both were non-uniform due to the continuously varying area.

One potential solution investigated was an indirect measurement of stress by using the load-displacement curve. The idea was that, using the load cell data and the corresponding crosshead displacement recorded by the testing machine, a load-displacement curve could be determined. Then, using the reduced notch area, load data could be converted to stress and compared to baseline results.

The main issue with this approach is that the output from the crosshead displacement is not suitable for comparison with the baseline data, which was acquired by using an extensometer in the elastic region of the stress-strain curve. Furthermore, if the elastic portions of the resulting curves for the notched specimens are not viable for comparison to the baseline, they in turn negatively impact the interpretation of the plastic data, as shown in Figure 25.

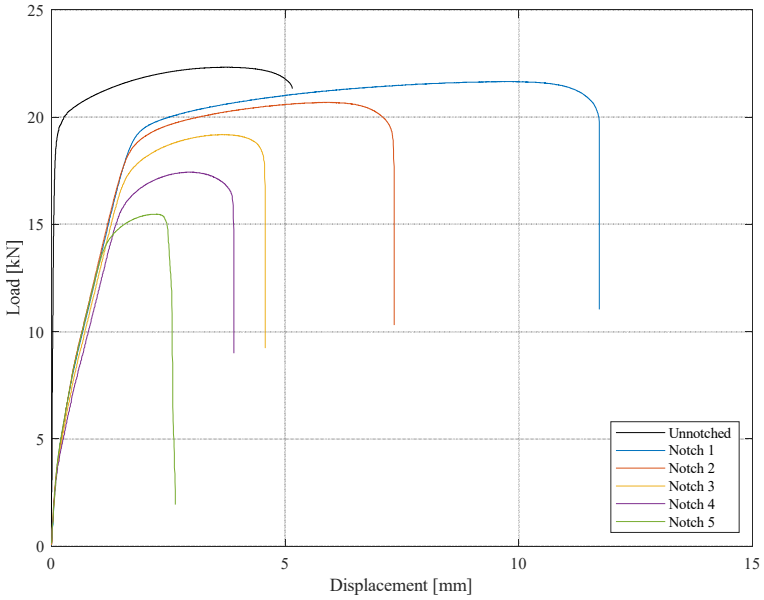

Figure 25. Load-Displacement Curves Using Crosshead Displacement. Crosshead displacement produces curves that cannot be adequately compared to the baseline.

In the interest of obtaining results for the notched samples that could be compared to the baseline, an extensometer was employed again to measure elastic displacement. The extensometer was placed in the middle of each tensile bar, with the prongs on either side of the notch, as shown below in Figure 26.

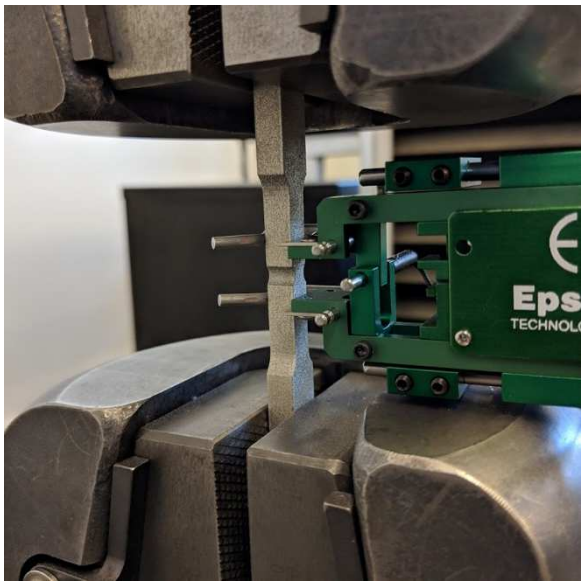

Figure 26. Experimental Setup for Notched Specimens. Similar to the baseline, an extensometer was used to measure elastic displacement.

This method is effective for high resolution elastic extension measurement of the notched samples, but converting from load-displacement to stress-stain is not straightforward. In the presence of a nonuniform cross-sectional area, a uniform stress-strain distribution in the notch region cannot be identified.

At first, it seemed intuitive that the appropriate area to use for stress determination would be the minimum reduced area at the notch, since the maximum local stress at that area is what drives the response of the sample. However, when that method is employed, the stress-strain curves shown in Figure 27 are produced as a result.

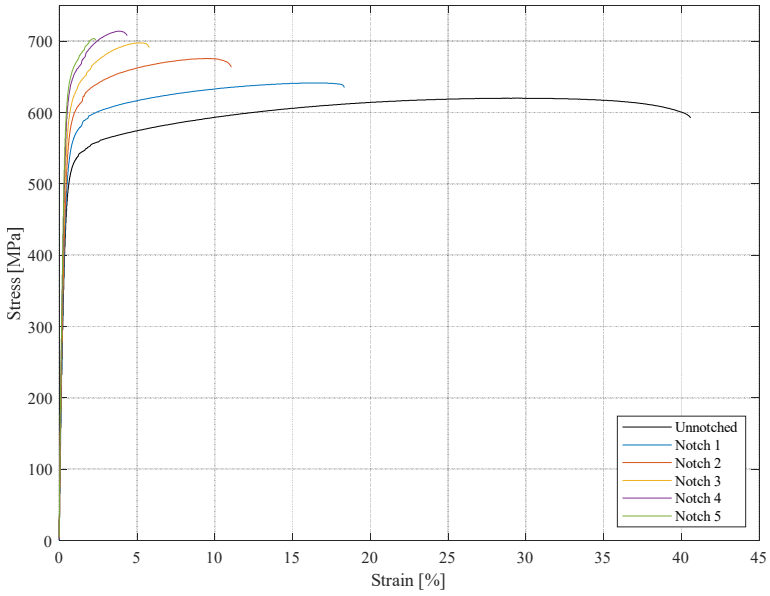

Figure 27. Stress-Strain Curves Created Using the Reduced Notch Area. Increased yield strengths are not consistent with the mechanics of stress concentrations in metals.

These curves suggest that an increase in strength should be expected from samples with notches included. Furthermore, this behavior suggests that the part becomes progressively stronger with deeper notches. However, such behavior would be illogical given the mechanics of stress concentrations. Thus, the minimum area was not used to determine the stress in the notched samples.

The next area investigated was the baseline area of the unnotched sample, 36mm^2. While this is not reflective of the actual geometry of the notched samples, it does have both qualitative and quantitative advantages. Since all measured loads were scaled by the same area, and the gauge length remained unchanged, the resulting stress-strain behavior was identical to the load-displacement behavior (both shown in Figure 28).

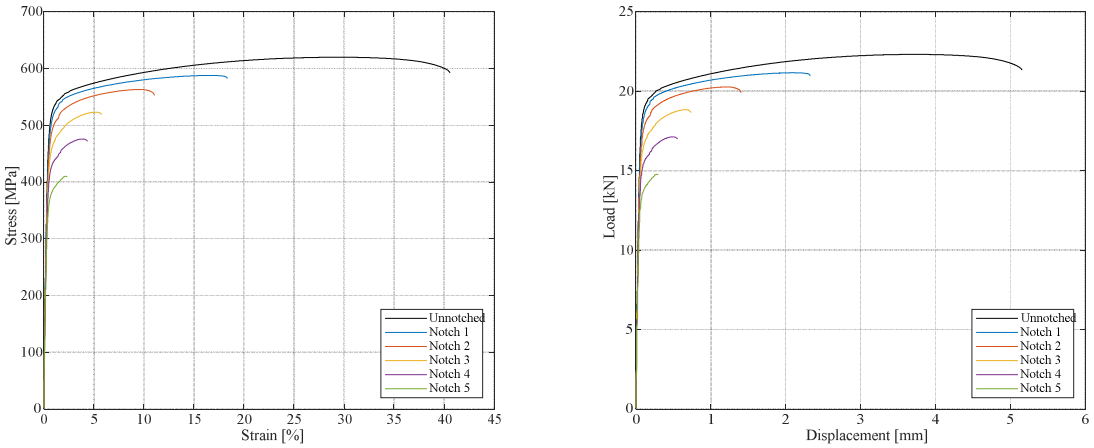

Figure 28. Comparison of Baseline Dimension Stress-Strain Curves with Load-Displacement Curves for Notched Specimens. Left: Curves derived using the baseline area for stress and the baseline gauge length for strain. Right: As-measured load-displacement curves for all specimens.

This approach makes possible a straightforward determination of the global yield loads using the 0.2% offset yield strength as calculated automatically by the tensile test program. These loads, listed below in Table 8, were later used as inputs to FEA models to understand the stress state for each notch at the onset of global yield. Load-displacement curves annotated with the yield point for each specimen are shown in Figure 29.

Table 8. Global Yield Loads. Loads correspond to the onset of global yield observedfor each sample.

Specimen/ Notch No.	Yield Load [kN]
0	16.8
1	16.1
2	15.3
3	14.9
4	14.0
5	12.6

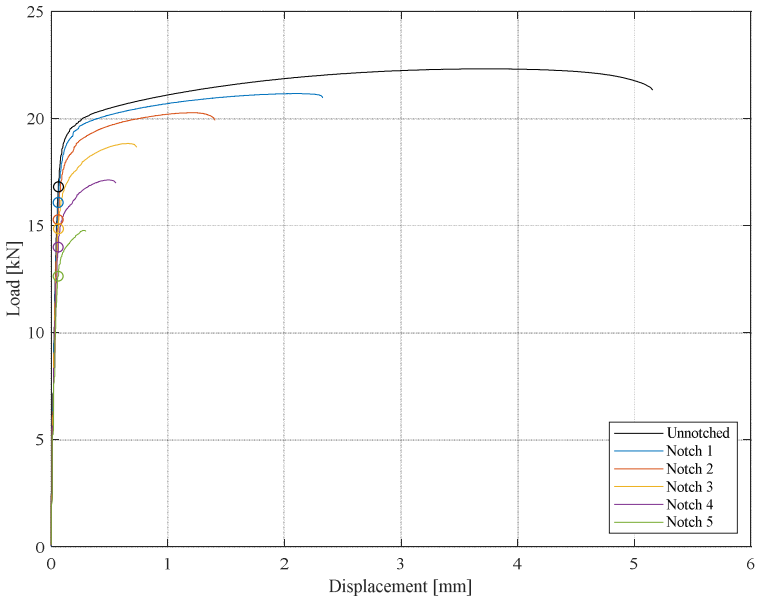

Figure 29. Annotated Load-Displacement Curves. Curves for baseline and notched tensile specimens shown, with the 0.2% offset global yield point indicated for each.

Examining this data, two overall trends can be identified. First, the load supported by each specimen is reduced with increasing notch depth. Second, as the net area of the notch is reduced, so is the total extension of the specimen.

4.4 FEA Results

4.4.1 Low Load Behavior

Using the tensile properties previously determined (Table 5) in conjunction with the plasticity behavior presented in Figure 20, Abaqus finite element models were employed to gain insight into the ideal yield stress state for each notch geometry. Stress visualization limits were set from 0 to 470MPa, the experimentally determined yield stress. Plastic deformation, i.e. stress in excess of 470MPa, is indicated in gray. Figure 30 demonstrates that, using a relatively low load, the models behave as expected. At roughly 8kN, which is just below 50% of the unnotched yield load determined from tensile testing, the unnotched model exhibits uniform stress on the order of

half the yield stress. Then, as the load is left unchanged but the notch geometry becomes progressively more severe, the local stress at the notch root also becomes more severe.

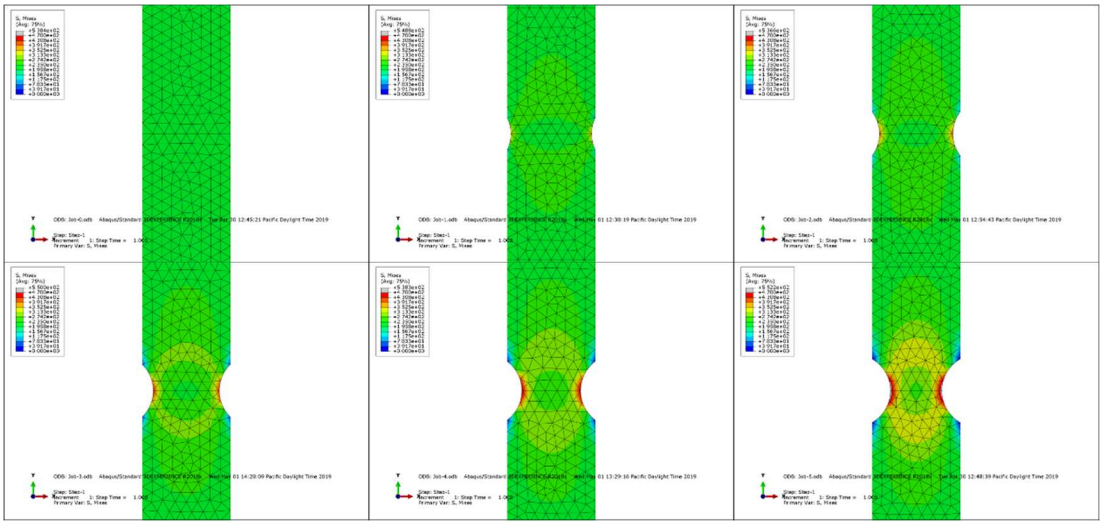

Figure 30. Low Load FEA. Finite element models with the same applied load for each specimen, generated with Abaqus. Front views indicate that the local stress concentration should grow as the notch deepens.

For the same load as shown in Figure 30 above, Figure 31 reveals the stress distribution in each model by observing a section view at an isometric angle. Note that for the load that produces only half the yield stress in the baseline sample, local plastic deformation is already developing in notches 4 and 5. This suggests that, for the ideal material, the global strength of the specimen should decrease as the notch severity increases.

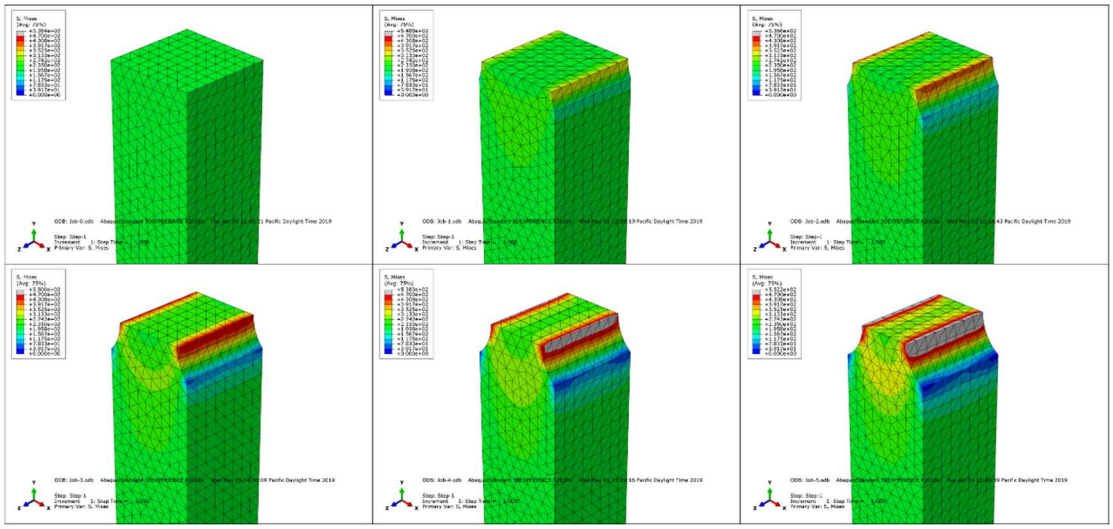

Figure 31. Isometric section FEA. Finite element models with the same applied load for each specimen, generated with Abaqus. Isometric section views reveal local yield, suggesting that global yield should occur at lower loads for deeper notches.

4.4.2 Global Yield Load Behavior

After examining the models with a low load, the global yield load for each geometry, determined through tensile testing, was applied (results shown in Figure 32). As with the low load application, the unnotched model again validates the approach, exhibiting uniform stress on the order of 470MPa, the empirically determined yield stress.

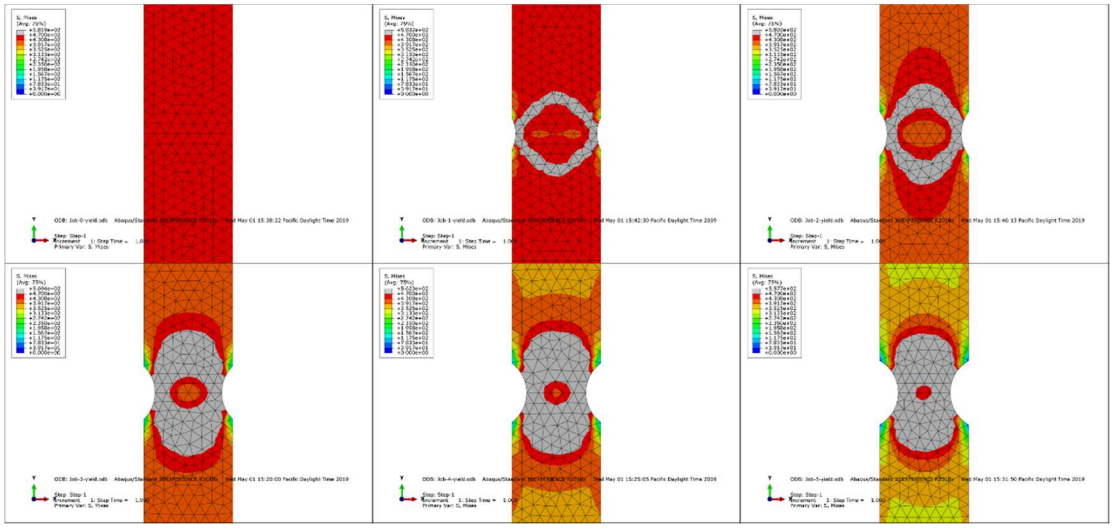

Figure 32. Global Yield Load FEA. Models with the respective global yield load applied for each specimen were generated with Abaqus. Shrinking elastic volume in the notched region suggests that the total remaining extension after global yield should diminish with notch depth.

As the notch grows deeper and the global yield load reduces, the FEA models produce interesting results. First, the amount of localized plastic deformation present at the onset of global yield is gradually increased, as indicated by the gray region surrounding the center of each sample. The increasing local plastic deformation occurs even as the global yield load decreases. The second observation of the FEA is the reduction in volume of elastic material available at the onset of global yield. This suggests that as the notch deepens, less additional strain energy can be retained at the reduced area beyond global yield. Taken together, these observations suggest that for the ideal material, the deeper the notch is, the less extension can be sustained by the specimen prior to fracture.

FEA results for the global yield loads are overlaid with the load-displacement curves from Figure 29 to create the juxtaposition in Figure 33. Observing them together, both of the trends in the experimental data are validated by the stress distributions observed in the FEA models. The notched SLM tensile bars exhibited plastic behavior congruent with the baseline plastic behavior of the unnotched specimen. That is, when the baseline true stress-strain constitutive relation from Figure 20 was applied to the finite element models, the predictions based on theoretical stress state at the global yield load matched the actual behavior in the test specimens. Thus, the static performance of the material is not inherently impacted by the porosity, surface condition, or other features of the as-printed state.

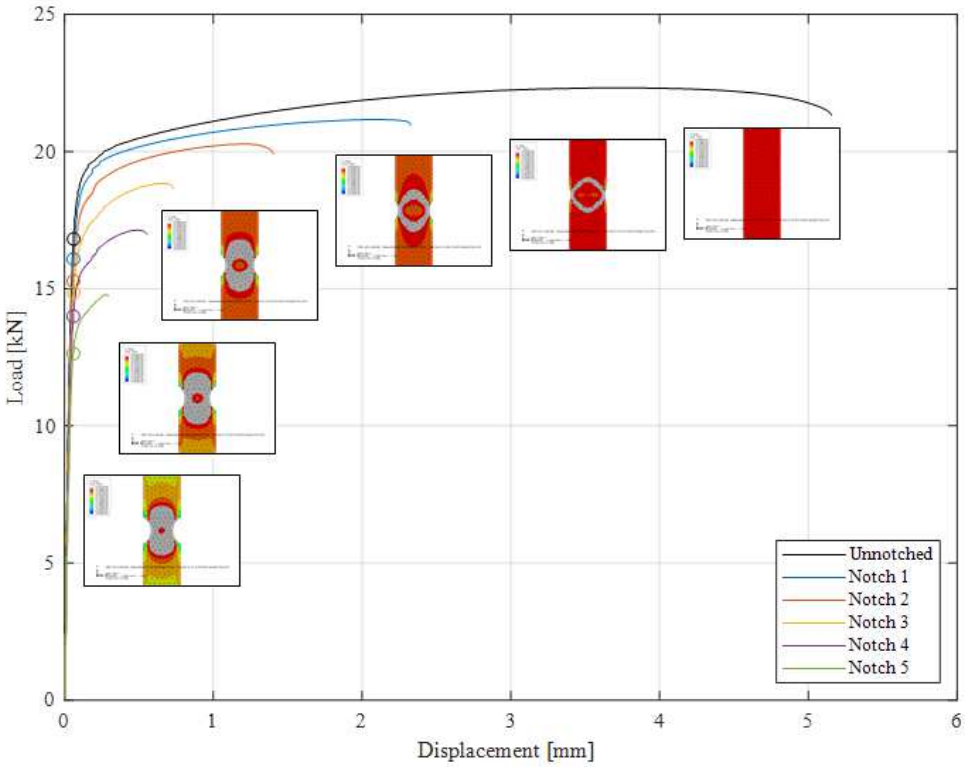

Figure 33. Theoretical and Experimental Behaviors. Experimental load-displacement curves with 0.2% offset global yield loads indicated, overlaid with FEA results for the stress state of each specimen at its respective yield load.

4.5 Fracture Behavior

4.5.1 Unnotched Failure

Ductile fracture was observed across all unnotched tensile bars geometries upon conclusion of the tests. Figure 34 shows an unnotched tensile bar that fractured following necking in the gauge length, characteristic of typical ductile failure.

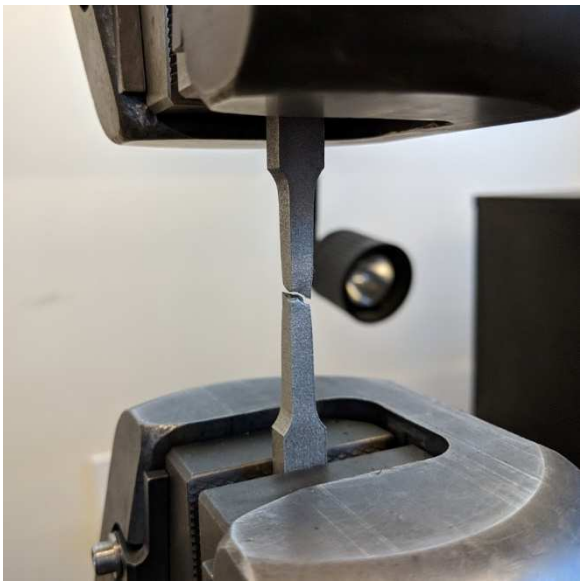

Figure 34. Conclusion of a Baseline Tensile Test. Necking exhibited in the gauge length is indicative of ductile failure.

Upon further examination, the fracture surface of the unnotched tensile bars exhibited unusual behavior. The macroscopic observations were checked by microscopic investigation, using a scanning electron microscope (SEM). Figure 35 shows images captured with a Thermo Scientific Quanta 200 SEM. Note the uniform distribution of porous features in the middle region of the fracture surface. A different fracture mechanism is observed at the outside border of the part, where there is a separate SLM laser scan pattern, but the global fracture appears to be dominated by the behavior at the center.

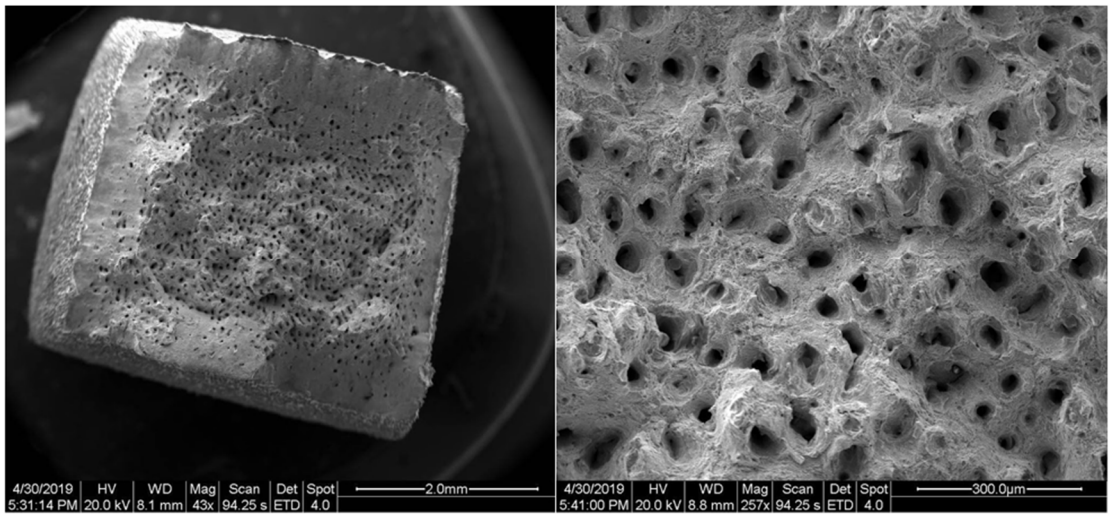

Figure 35. SEM Images of a Fractured Baseline Specimen. Uniform porous features suggest that the fracture mechanics are artificial. Left: The entire fracture surface. Right: Detail view of porous features.

4.5.2 Notched Failure

Roughly the same behavior was observed in the notched tensile bars as in the unnotched samples. Figure 36 shows images of fractures that occurred as expected in the notches at the locations where the area is most reduced, corresponding to high localized stress.

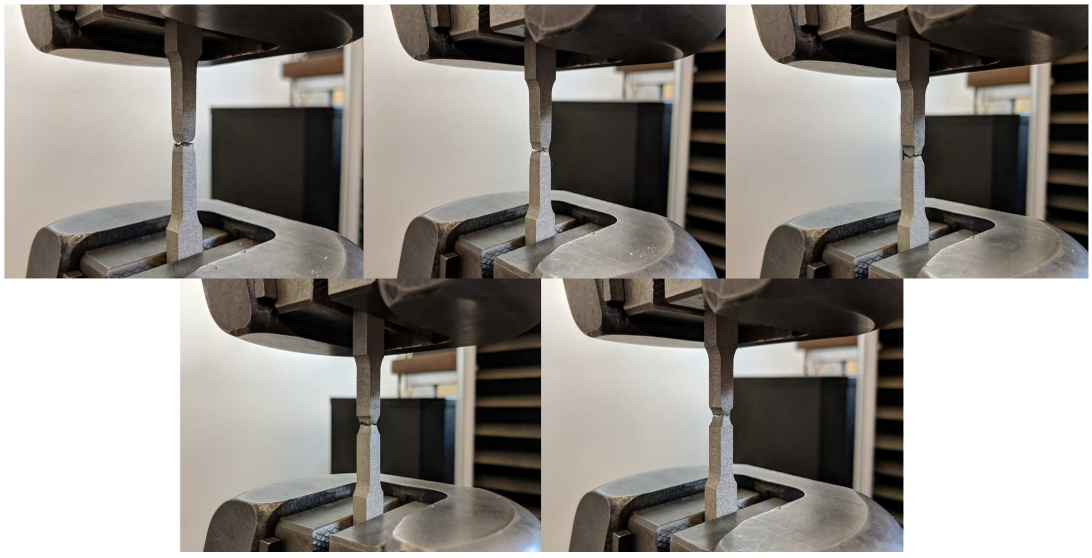

Figure 36. Conclusions of Notched Tensile Tests. Note that failure occurred in the notched region, as expected. Top row: Notches 1-3. Bottom row: Notches 4 and 5.

An SEM investigation of notch 5, which was the most severe notch geometry, revealed that the notch fracture behavior was somewhat similar to the unnotched behavior. The images included below in Figure 37 show that the fracture surface of notch 5 demonstrates the same porous features seen on the unnotched fracture surface. Note that the edges near the notch root appear to exhibit porosity with shape and distribution resembling the unnotched behavior, whereas the middle of the fracture surface appears to distinctly reveal the laser scan pattern, which is somewhat less discernible in the unnotched specimen.

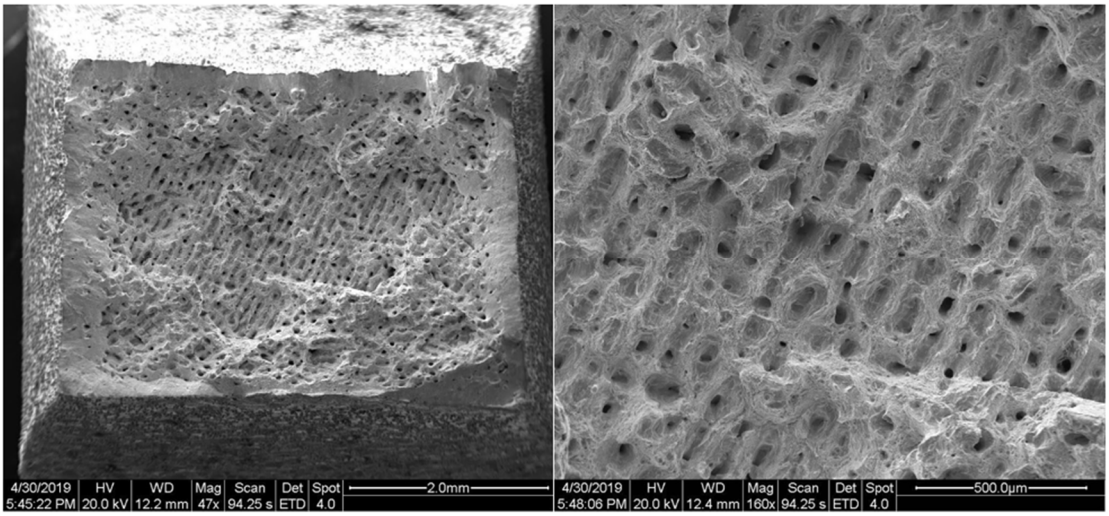

Figure 37. SEM Images of the Fracture Surface in a Notch 5 Specimen. Ductile behavior similar to the baseline is observed again in the notch. Left: The entire fracture surface, which appears to reveal the laser scan pattern. Right: Detail view of ductile features.

4.5.3 Defect-Driven Failure

Other than the parts that experienced the print interruption previously mentioned, only one tensile specimen was conclusively defective. Below in Figure 38, a photo of a notched tensile bar that failed prematurely away from the notch is shown. Further inspection using the SEM revealed the presence of unmelted powder at the fracture surface. Several others, such as Liverani, et. al [10], have also observed this binding defect, which provides an internal material discontinuity whereby the premature failure begins. It is not known why this defect was witnessed in this particular sample only and not others from the same build, nor is the mechanism well understood

by which partial melting occurs while near-full density is also observed for identical SLM parameters.

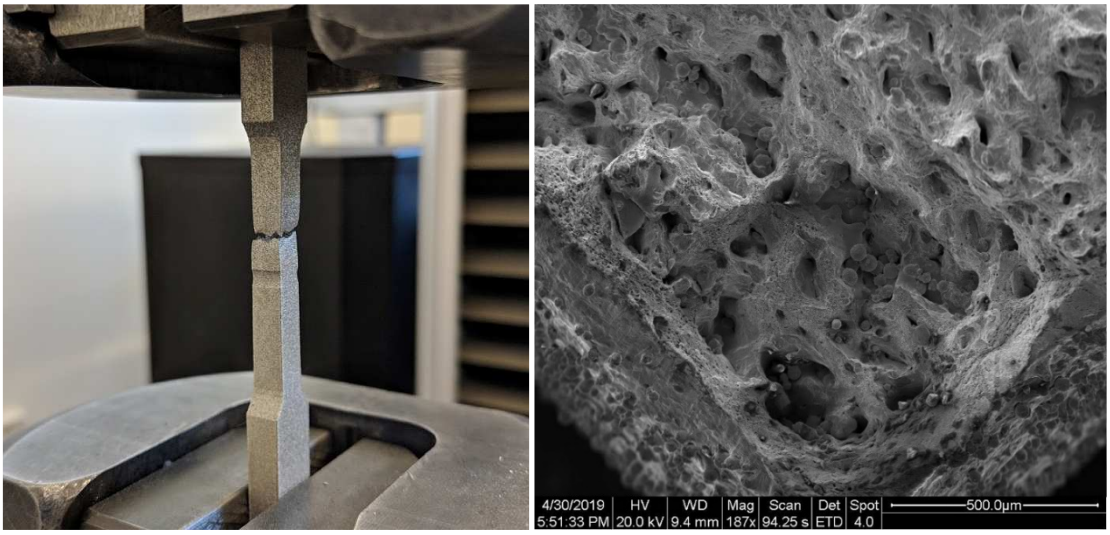

Figure 38. Images of the Only Conclusively Defective Specimen. Left: Failure occurred away from the notch. Right: SEM investigation revealed that unmelted powder was likely the root cause of failure.

4.6 Further Investigation of Non-Defective Fractures

4.6.1 Mechanism for Ductile Pore Formation

While the necking behavior of the unnotched test specimens suggested that the failure was ductile, the fracture surface did not appear to resemble traditional ductile failure. Song, et. al [17] demonstrated that ductile failure of 316L should exhibit a somewhat random distribution of interconnected parabolic dimple features, shown in Figure 39.

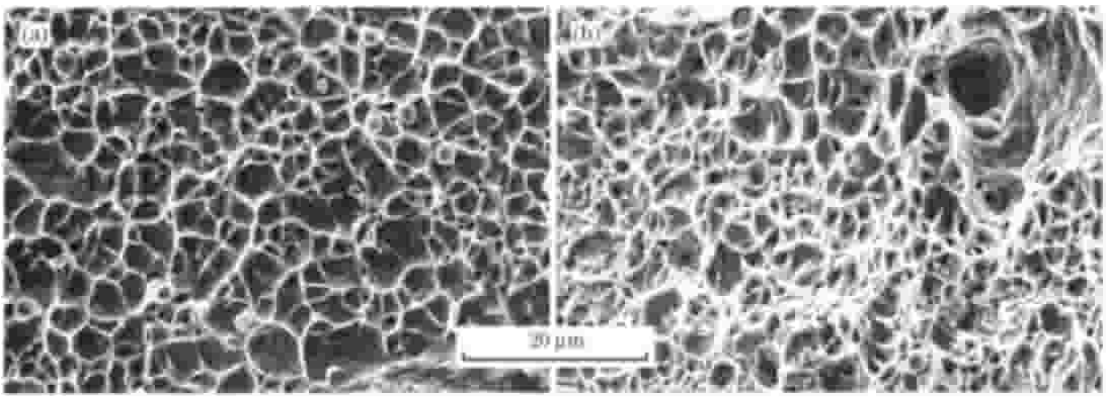

Figure 39. Ductile Fracture Structures. SEM images of ductile fracture structures in 316L stainless steel, published by Song, et. al [17]. Left: hot rolled. Right: Solution-treated.

Following the observation of this discrepancy, the apparent porosity revealed after fracture was examined further to investigate possible explanations. Cooper, et. al [18] observed similar porous structures in 316L tension specimens treated by hot isostatic pressing (HIP). Their research suggested that the mechanism for the formation of such voids was the presence of non-metallic oxide inclusions, which provide microscopic stress concentration sites whereby microvoids initiate during plastic deformation. An SEM image from their research is provided in Figure 40. Note that there does not appear to be any regularity to the distribution of voids.

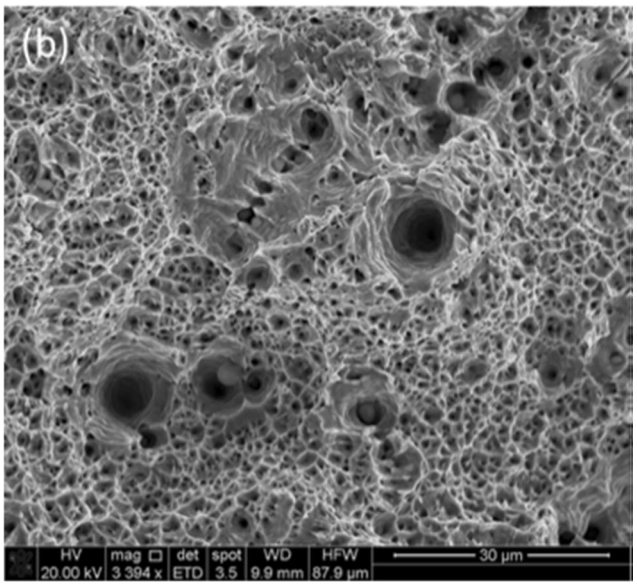

Figure 40. SEM Image of Oxide Pores. Work published by Cooper, et. al [18] showed a fracture surface in hot isostatically pressed 316L containing large oxide pore features.

An important finding from the work by Cooper, et. al was that the strength of the HIP-ed 316L was not affected by the oxygen content in the base material. The presence of the non-metallic oxides, which provided the mechanism for ductile pore formation, was not found to have a negative impact on the tensile properties compared to a forged reference material. Furthermore, significant variance in the oxygen content of the 316L base material had little effect on the resulting yield and tensile strengths, as shown by their summary in Figure 41. The first set of columns represents the as-forged reference properties, while sets of columns to the right represent samples with increasing oxide content. Cooper, et. al note that the content of nitrogen, a strengthening element, in material HIP100A did not meet ASTM specification.

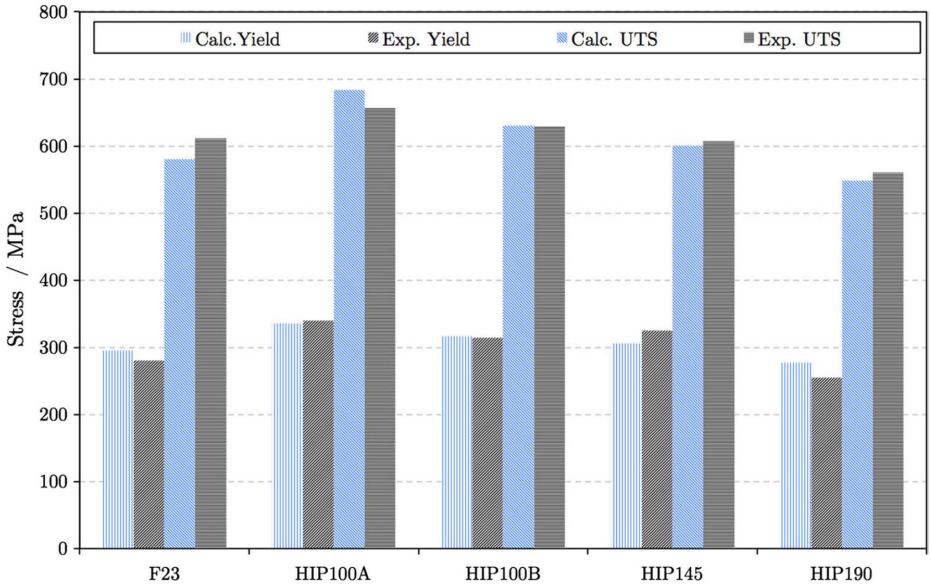

Figure 41. Strengths of HIP-ed 316L. Results from Cooper, et. al [18] showing that the strengths of hot isostatically pressed 316L tensile samples was not significantly affected by varying oxide content.

4.6.2 Mechanism for Ductile Pore Distribution

After identifying a potential mechanism for the creation of pores, identification of a separate mechanism for the apparent regular distribution of pores was pursued. Using ImageJ, the SEM image was converted to a binary image so that the spacing of the pores could be analyzed. The progression of the image processing is presented in Figure 42. After the pores were identified, the Nearest Neighbor Distance plugin for ImageJ was used to approximate the average spacing between pore centroids, which was calculated to be about 68μm.

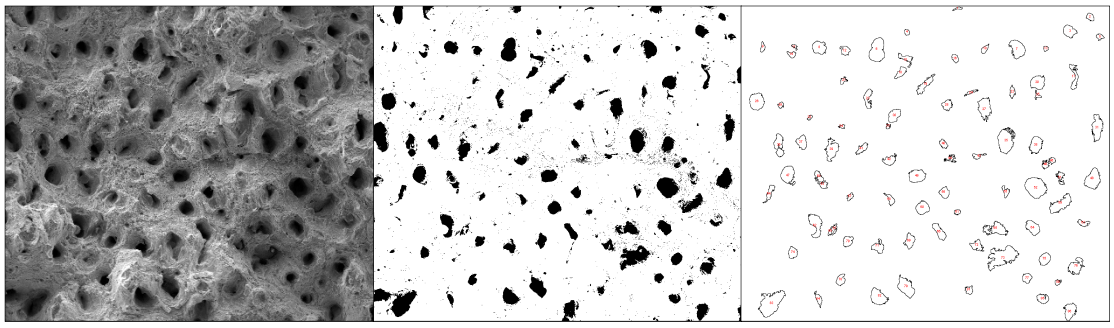

Figure 42. Unnotched ImageJ analysis. Left: original unnotched SEM image. Middle: binary black and white image. Right: pores in the unnotched binary image as identified by ImageJ.

The same image processing recipe was followed for the notched SEM image, and the progression of that analysis is shown in Figure 43. For that case, the approximate average distance between pore centroids was calculated to be 85μm. It was observed that the laser scan pattern had a larger influence on the pore geometry for the notched specimen, creating elongated pores in the direction of the laser scan, which in turn affected the calculated average spacing. Nevertheless, the distribution of the pores in the notched specimen was still roughly on the same order as that of the unnotched specimen, suggesting that they relied on the same mechanism for their formation. A summary of the porosity analysis is given in Table 9. Note that the SEM images for the unnotched and notched fracture surfaces were taken at 257x and 160x magnifications, respectively.

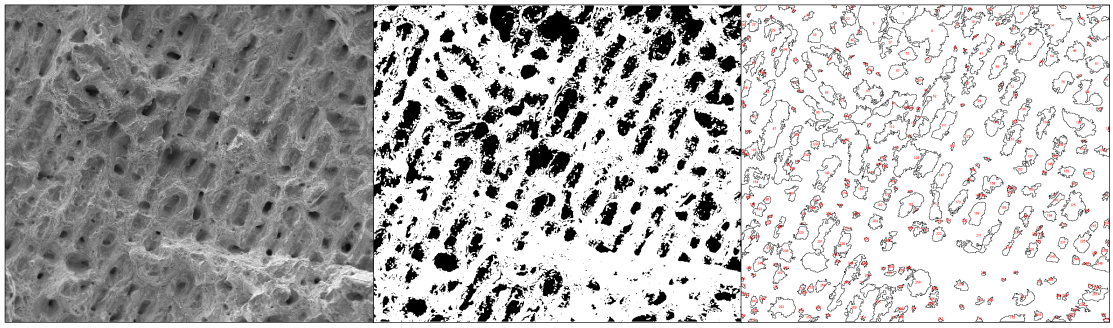

Figure 43. Notch 5 ImageJ analysis. Left: original unnotched SEM image. Middle: binary black and white image. Right: pores in the notched binary image as identified by ImageJ.

Table 9. Summary of ImageJ Porosity Analysis.

SEM Image	Average Pore Spacing [μm]	Standard Deviation [μm]
Unnotched	68	24
Notch 5	85	37

Recall from Pohl's results in Table 1 that the hatching distance was set to 120µm, and the spot size of the laser was 70µm. Note that the average pore spacing in the unnotched sample was on the order of roughly half the hatching distance, and almost exactly equal to the laser spot size. Using these dimensions, a sketch was created in Solidworks to help visualize the scan pattern, which is shown in Figure 44. Note the scan direction for each layer, indicated by the colored arrows.

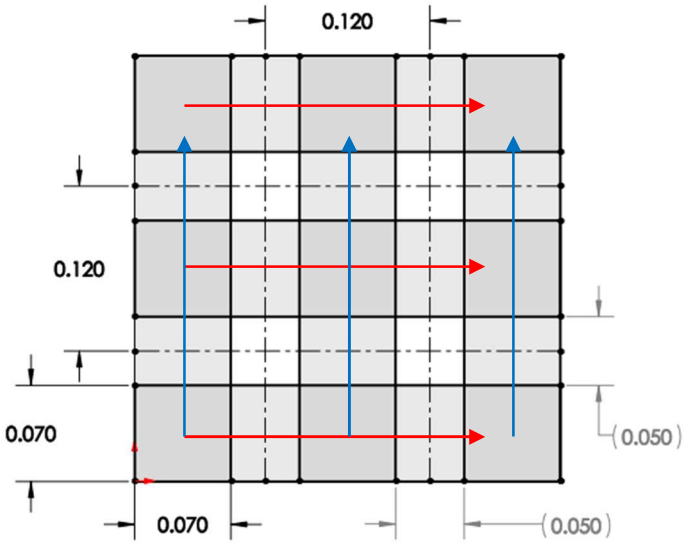

Figure 44. Scan Pattern Illustration. Given the dimensions of the laser spot and the hatching distance (shown in mm), a uniform distribution of unmelted particles could be created.

When subsequent layer scans are rotated by 90°, the current SLM parameters leave a uniform scatter of unmelted powder in squares 50µm wide and 120µm apart in both X and Y. An important caveat to note is that the scans illustrated in Figure 44 are offset at 90°, whereas Pohl's settings rotate subsequent layers by 33°. Therefore the exact size and shape of the unmelted scatter, if any, is bound to be different from this approximation. Still, this visualization suggests that there might be a mechanism for regular or semi-regular distribution of internal print features created as a result of the combined laser spot size and hatching distance parameters.

Even if near-complete melting is achieved by the SLM settings, the scan pattern would still create a somewhat uniform distribution of weld pool interfaces, which could provide a mechanism for the scatter of non-metallic oxides in the part. More work will need to be done to characterize the chemistry of the 316L powder in the as-received and recycled conditions to quantify oxygen concentrations. A deeper investigation of the fracture surfaces is also needed in order to confirm that the ductile pores occur at locations where oxides have settled in the material. Furthermore, experimenting with different scan parameters could help identify any influence on the distribution of ductile pores in the fracture surfaces of as-printed specimens.

5. CONCLUSION AND RECOMMENDATIONS

5.1 Conclusion

Tensile testing was conducted to provide the material properties of as-printed 316L stainless steel samples produced using selective laser melting. In order to have confidence in the experimental results, other investigations also needed to be conducted to validate previous assumptions. Stereological relative density measurements showed that the as-printed material exhibited relative density in excess of 99%. Optical dimensional analysis found that the as-printed tensile specimens met ASTM E8 dimensional requirements in 14 out of 15 parts inspected. Baseline tensile tests indicated that the yield stress of the as-printed material is 24% higher than a cold-rolled alternative, while still achieving comparable ductility. The location of a tensile specimen on the build plate during the print was not found to have a significant effect on its mechanical properties. Notched tensile specimens of varying notch depths were tested to obtain experimental load-displacement curves. A 0.2% offset global yield load was determined for each specimen and applied to their respective finite element models. Theoretical predictions based on the model behavior matched experimental behavior in the actual specimens. Unique fracture behavior was found in both the unnotched reference and the most severe notch after SEM inspection, and a root cause related to oxide distributions was proposed. After extrapolating from previous studies and observing that experimental results matched theoretical models, it was determined that features inherent to SLM parts were not detrimental to the static performance of the as-printed material.

5.2 Recommendations

During the location dependence testing, the print paused when the SLM ran out of powder, creating parts with a critical defect at that layer. It was theorized that if the SLM was configured to use less total powder per layer (i.e. less waste) while still demonstrating comparable material properties, then perhaps that type of printing error could be avoided for tall parts. Density measurements conducted for such a configuration revealed that relative densities above 99% were

still achievable, but no further testing has been pursued as of yet. Establishing a static baseline for these settings would still be useful for design even if the resulting properties are not comparable to the previous data.

Preliminary work has already been done at Cal Poly by Andrew Yap to characterize the performance of the SLM material in the annealed condition, following post-print treatment. As was the case with the as-printed material, initial properties of annealed SLM 316L seem to provide a compelling alternative to other available options. A broad trade study that compares the SLM material treated with various traditional heat treatments to other known alternatives would be valuable. This information could be used to more comprehensively identify design spaces where current capabilities are inadequate, but SLM might be a viable solution.

Further investigation of the fracture surfaces of SLM tensile samples is also warranted. To validate the proposed root cause of the ductile pore formation, further SEM analysis is required. Chemical composition analysis of the 316L powder in the as-received and recycled conditions is needed to quantify oxygen content. A thorough parametric study that varies laser spot size and hatching distance would confirm the mechanism that controls the distribution of the ductile pores.

It has been demonstrated that features inherent to the as-printed SLM material are not detrimental to its static performance. However, additional investigation is required to evaluate the impact that these features will have on dynamic performance. Furthermore, it would be valuable for design to characterize the dynamic performance of material in the as-printed condition based on experimental data. The Materials Engineering department at Cal Poly has equipment capable of fully-reversed bending fatigue testing, and as-printed SLM coupons have already been proven to be compatible with the apparatus without the need for post-machining, shortening the feedback loop. Results could be used to supplement existing published data or for comparison to results for uniaxial tension fatigue and checked for agreement across methods.

REFERENCES

[1] Wohlers, Terry T., and Tim Gornet. “History of Additive Manufacturing.” *Wohlers Report 2014: 3D Printing and Additive Manufacturing State of the Industry Annual Worldwide Progress Report*, Wohlers Associates, 2014, pp. 1–34.

[2] Sun, Zhongji, et al. “Selective Laser Melting of Stainless Steel 316L with Low Porosity and High Build Rates.” *Materials & Design*, vol. 104, 2016, pp. 197–204., doi:10.1016/j.matdes.2016.05.035.

[3] Li, Ruidi, et al. “Densification Behavior of Gas and Water Atomized 316L Stainless Steel Powder during Selective Laser Melting.” *Applied Surface Science*, vol. 256, no. 13, 2010, pp. 4350–4356., doi:10.1016/j.apsusc.2010.02.030.

[4] Kruth, J. P., et al. “Part and Material Properties in Selective Laser Melting of Metals.” *16th International Symposium on Electromachining (ISEM - XVI) ; Shanghai, China, 19-23 April 2010*, Curran, 2014.

[5] Kruth, J. “Selective Laser Melting of Iron-Based Powder.” *Journal of Materials Processing Technology*, 2004, doi:10.1016/s0924-0136(04)00220-1.

[6] Wu, Amanda S., et al. “An Experimental Investigation into Additive Manufacturing-Induced Residual Stresses in 316L Stainless Steel.” *Metallurgical and Materials Transactions A*, vol. 45, no. 13, 2014, pp. 6260–6270., doi:10.1007/s11661-014-2549-x.

[7] Kamath, Chandrika, et al. “Density of Additively-Manufactured, 316L SS Parts Using Laser Powder-Bed Fusion at Powers Up to 400W.” *Metallurgical and Materials Transactions A*, vol. 45A, Dec. 2014, pp. 6260–6270., doi:10.2172/1116929.

[8] Pohl, Sebastian. “Improving Printing Quality by Optimizing Linear Energy Density in Selective Laser Melting and Demonstrating Its Inherent Constraints.” *Munich University of Applied Sciences*, 2019.

[9] ASTM Standard E8/E8M, 2016a, "Standard Test Methods for Tension Testing of Metallic Materials," ASTM International, West Conshohocken, PA, 2016, doi: 10.1520/E0008_E0008M-16A

[10] Liverani, E., et al. “Effect of Selective Laser Melting (SLM) Process Parameters on Microstructure and Mechanical Properties of 316L Austenitic Stainless Steel.” *Journal of Materials Processing Technology*, vol. 249, 2017, pp. 255–263., doi:10.1016/j.jmatprotec.2017.05.042.

[11] Spierings, A.b., et al. “Comparison of Density Measurement Techniques for Additive Manufactured Metallic Parts.” *Rapid Prototyping Journal*, vol. 17, no. 5, 2011, pp. 380–386., doi:10.1108/13552541111156504.

[12] ASTM Standard B311, 2017, Standard Test Method for Density of Powder Metallurgy (PM) Materials Containing Less Than Two Percent Porosity," ASTM International, West Conshohocken, PA, 2017, doi: 10.1520/B0311-17

[13] “AISI Type 316L Stainless Steel, Annealed Bar.” *MatWeb*, www.matweb.com/search/DataSheet.aspx?MatGUID=a2d0107bf958442e9f8db6dc9933fe31&ckck=1.

[14] “AISI Type 316L Stainless Steel, Annealed and Cold Drawn Bar.” *MatWeb*, www.matweb.com/search/DataSheet.aspx?MatGUID=c02b8c0ae42e459a872553e0ebfab648.

[15] Wang, Y. Morris, et al. “Additively Manufactured Hierarchical Stainless Steels with High Strength and Ductility.” *Nature Materials*, vol. 17, no. 1, 30 Oct. 2017, pp. 63–71., doi:10.1038/nmat5021.

[16] Fitzgerald, E., and W. Everhart. “The Effect of Location on the Structure and Mechanical Properties of Selective Laser Melted 316L Stainless Steel.” University of Texas, Proceedings of the 27th Annual International Solid Freeform Fabrication Symposium 2016: an Additive Manufacturing Conference, August 8-10, 2016, the University of Texas at Austin, Austin, Texas, USA, 2016, pp. 574–583.

[17] Song, Ren-Bo, et al. “Characteristics of Mechanical Properties and Microstructure for 316L Austenitic Stainless Steel.” *Journal of Iron and Steel Research International*, vol. 18, no. 11, 2011, pp. 53–59., doi:10.1016/s1006-706x(11)60117-9.

[18] Cooper, A. J., et al. “Tensile Fracture Behavior of 316L Austenitic Stainless Steel Manufactured by Hot Isostatic Pressing.” *Metallurgical and Materials Transactions A*, vol. 49, no. 5, 2018, pp. 1579–1591., doi:10.1007/s11661-018-4518-2.

Appendix A: Engineering Drawings of Tensile Specimens

NOTES:
-ALL DIMENSIONS AND TOLERANCES
IN MM PER ASTM E8 (SUBSIZE SPECIMEN)

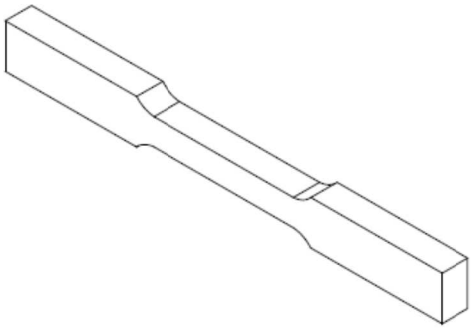

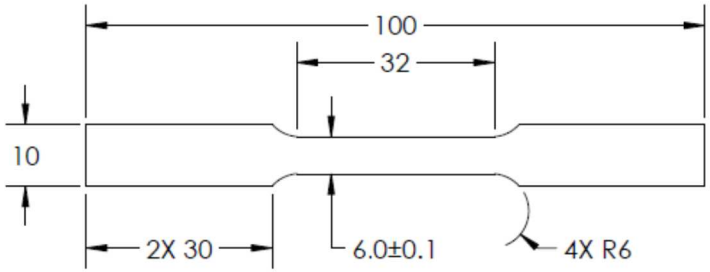

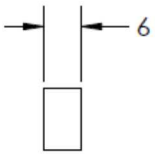

Cal Poly Mechanical Engineering ME 599 - Thesis	Title: Specimen 0 Date: 2/20/19	Scale: 1:1 Material: 316L SS	Drawn by: Paul Swartz	Advisors: Thomas Mackin, Xuan Wang

NOTES:
-ALL DIMENSIONS AND TOLERANCES
IN MM PER ASTM E8 (SUBSIZE SPECIMEN)

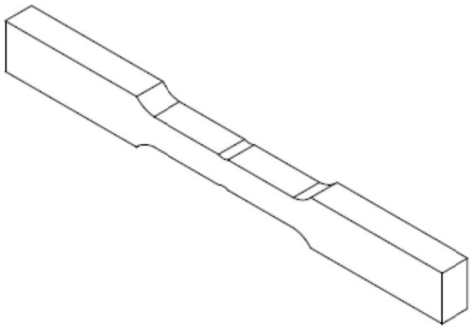

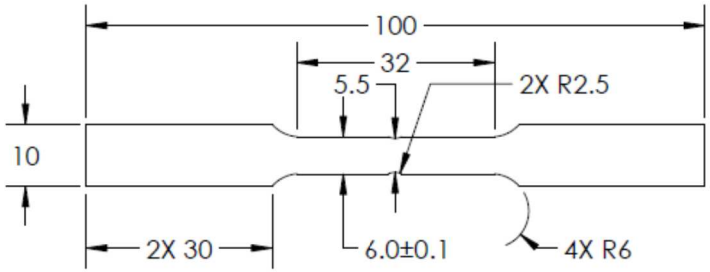

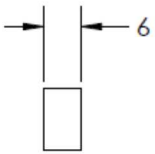

Cal Poly Mechanical Engineering ME 599 - Thesis	Title: Specimen 1 Date: 2/20/19	Scale: 1:1 Material: 316L SS	Drawn by: Paul Swartz	Advisors: Thomas Mackin, Xuan Wang

NOTES:
-ALL DIMENSIONS AND TOLERANCES
IN MM PER ASTM E8 (SUBSIZE SPECIMEN)

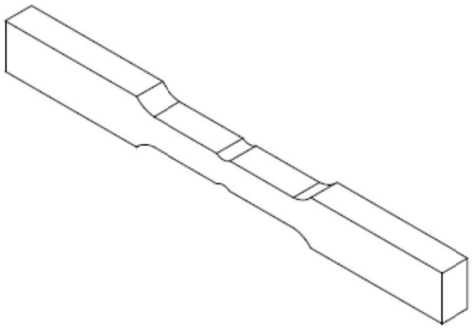

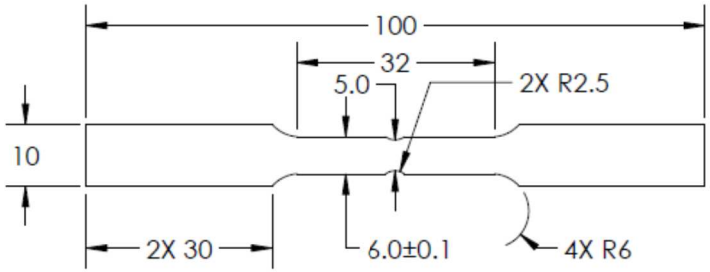

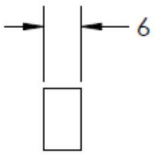

Cal Poly Mechanical Engineering ME 599 - Thesis	Title: Specimen 2 Date: 2/20/19	Scale: 1:1 Material: 316L SS	Drawn by: Paul Swartz	Advisors: Thomas Mackin, Xuan Wang

NOTES:
-ALL DIMENSIONS AND TOLERANCES
IN MM PER ASTM E8 (SUBSIZE SPECIMEN)

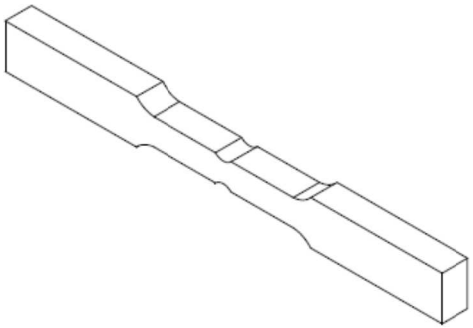

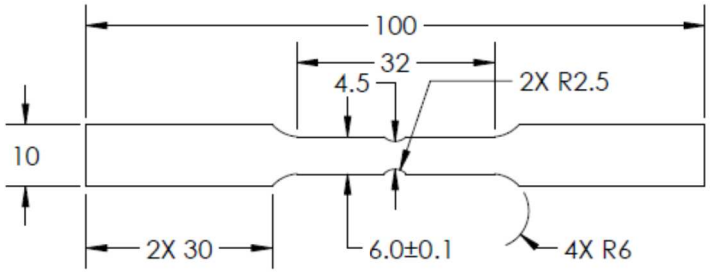

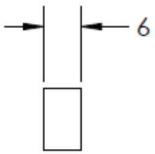

Cal Poly Mechanical Engineering ME 599 - Thesis	Title: Specimen 3 Date: 2/20/19	Scale: 1:1 Material: 316L SS	Drawn by: Paul Swartz	Advisors: Thomas Mackin, Xuan Wang

NOTES:
-ALL DIMENSIONS AND TOLERANCES
IN MM PER ASTM E8 (SUBSIZE SPECIMEN)

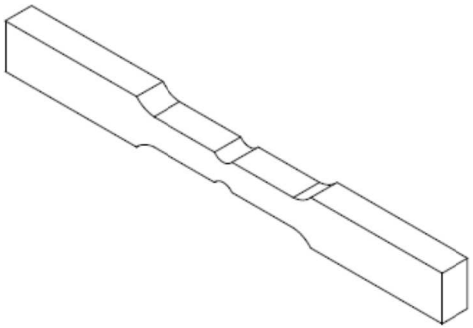

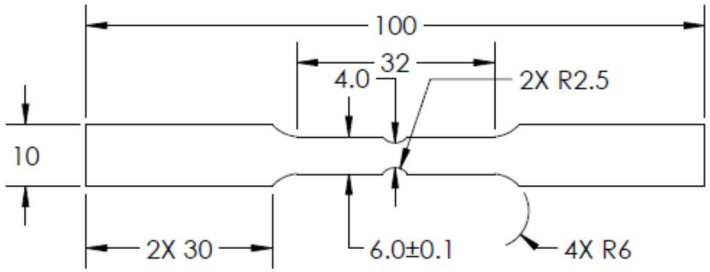

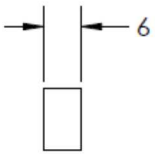

Cal Poly Mechanical Engineering ME 599 - Thesis	Title: Specimen 4 Date: 2/20/19	Scale: 1:1 Material: 316L SS	Drawn by: Paul Swartz	Advisors: Thomas Mackin, Xuan Wang

NOTES:
-ALL DIMENSIONS AND TOLERANCES
IN MM PER ASTM E8 (SUBSIZE SPECIMEN)

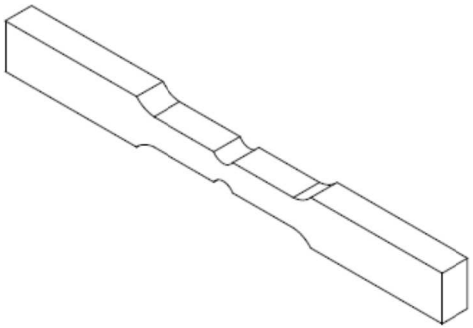

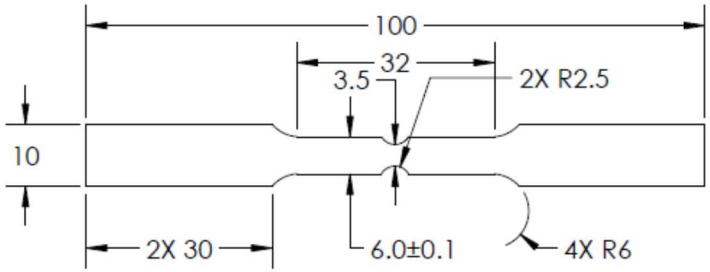

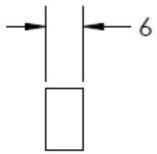

Cal Poly Mechanical Engineering ME 599 - Thesis	Title: Specimen 5 Date: 2/20/19	Scale: 1:1 Material: 316L SS	Drawn by: Paul Swartz	Advisors: Thomas Mackin, Xuan Wang

Appendix B: Dimensional Analysis Raw Data

Program: SLM tension samples.iwp Date: Wed Apr 10 2019 Time: 16:09:07
Units: mm, dec deg

Feature	Actual	Nominal	Upper	Lower	Dev/Nom	Out/Tol
Distance A	[System 5]					
Distance Y	10.0809	10.0000	0.0000	0.0000	0.0809	0.0809
Distance B	[System 5]					
Distance Y	10.1088	10.0000	0.0000	0.0000	0.1088	0.1088
Arc C	[System 5]					
Radius	6.1704	6.0000	0.0000	0.0000	0.1704	0.1704
Arc D	[System 5]					
Radius	5.8353	6.0000	0.0000	0.0000	-0.1647	-0.1647
Arc E	[System 5]					
Radius	5.8056	6.0000	0.0000	0.0000	-0.1944	-0.1944
Arc F	[System 5]					
Radius	5.6447	6.0000	0.0000	0.0000	-0.3553	-0.3553
Distance H	[System 5]					
Distance Y	6.0621	6.0000	0.1000	-0.1000	0.0621	
Distance I	[System 5]					
Distance X	30.0518	30.0000	0.0000	0.0000	0.0518	0.0518
Distance J	[System 5]					
Distance X	30.3605	30.0000	0.0000	0.0000	0.3605	0.3605
Plane K	[System 5]					
Flatness	0.3079		0.0000			0.3079

Program: SLM tension samples.iwp Date: Wed Apr 10 2019 Time: 16:11:57
Units: mm, dec deg

Feature	Actual	Nominal	Upper	Lower	Dev/Nom	Out/Tol
Distance A	[System 5]					
Distance Y	10.0465	10.0000	0.0000	0.0000	0.0465	0.0465
Distance B	[System 5]					
Distance Y	10.0419	10.0000	0.0000	0.0000	0.0419	0.0419
Arc C	[System 5]					
Radius	5.4225	6.0000	0.0000	0.0000	-0.5775	-0.5775
Arc D	[System 5]					
Radius	6.0258	6.0000	0.0000	0.0000	0.0258	0.0258
Arc E	[System 5]					
Radius	6.0118	6.0000	0.0000	0.0000	0.0118	0.0118
Arc F	[System 5]					
Radius	6.1692	6.0000	0.0000	0.0000	0.1692	0.1692
Distance H	[System 5]					
Distance Y	6.0378	6.0000	0.1000	-0.1000	0.0378	
Distance I	[System 5]					
Distance X	30.0555	30.0000	0.0000	0.0000	0.0555	0.0555
Distance J	[System 5]					
Distance X	30.2999	30.0000	0.0000	0.0000	0.2999	0.2999
Plane K	[System 5]					
Flatness	0.2717		0.0000			0.2717

Program: SLM tension samples.iwp Date: Wed Apr 10 2019 Time: 16:14:37
Units: mm, dec deg

Feature	Actual	Nominal	Upper	Lower	Dev/Nom	Out/Tol
Distance A	[System 5]					
Distance Y	10.0781	10.0000	0.0000	0.0000	0.0781	0.0781
Distance B	[System 5]					
Distance Y	10.0718	10.0000	0.0000	0.0000	0.0718	0.0718
Arc C	[System 5]					
Radius	5.5954	6.0000	0.0000	0.0000	-0.4046	-0.4046
Arc D	[System 5]					
Radius	6.0674	6.0000	0.0000	0.0000	0.0674	0.0674
Arc E	[System 5]					
Radius	5.3272	6.0000	0.0000	0.0000	-0.6728	-0.6728
Arc F	[System 5]					
Radius	6.1003	6.0000	0.0000	0.0000	0.1003	0.1003
Distance H	[System 5]					
Distance Y	6.0715	6.0000	0.1000	-0.1000	0.0715	
Distance I	[System 5]					
Distance X	30.0797	30.0000	0.0000	0.0000	0.0797	0.0797
Distance J	[System 5]					
Distance X	30.3644	30.0000	0.0000	0.0000	0.3644	0.3644
Plane K	[System 5]					
Flatness	0.3010		0.0000			0.3010

Program: SLM tension samples.iwp Date: Wed Apr 10 2019 Time: 16:16:44
Units: mm, dec deg

Feature	Actual	Nominal	Upper	Lower	Dev/Nom	Out/Tol
Distance A	[System 5]					
Distance Y	10.0720	10.0000	0.0000	0.0000	0.0720	0.0720
Distance B	[System 5]					
Distance Y	10.0900	10.0000	0.0000	0.0000	0.0900	0.0900
Arc C	[System 5]					
Radius	6.0036	6.0000	0.0000	0.0000	0.0036	0.0036
Arc D	[System 5]					
Radius	5.9182	6.0000	0.0000	0.0000	-0.0818	-0.0818
Arc E	[System 5]					
Radius	5.7496	6.0000	0.0000	0.0000	-0.2504	-0.2504
Arc F	[System 5]					
Radius	5.3697	6.0000	0.0000	0.0000	-0.6303	-0.6303
Distance H	[System 5]					
Distance Y	6.0700	6.0000	0.1000	-0.1000	0.0700	
Distance I	[System 5]					
Distance X	30.1436	30.0000	0.0000	0.0000	0.1436	0.1436
Distance J	[System 5]					
Distance X	30.2810	30.0000	0.0000	0.0000	0.2810	0.2810
Plane K	[System 5]					
Flatness	0.3012		0.0000			0.3012

Program: SLM tension samples.iwp Date: Wed Apr 10 2019 Time: 16:19:39
Units: mm, dec deg

Feature	Actual	Nominal	Upper	Lower	Dev/Nom	Out/Tol
Distance A	[System 5]					
Distance Y	10.0500	10.0000	0.0000	0.0000	0.0500	0.0500
Distance B	[System 5]					
Distance Y	10.0824	10.0000	0.0000	0.0000	0.0824	0.0824
Arc C	[System 5]					
Radius	6.2819	6.0000	0.0000	0.0000	0.2819	0.2819
Arc D	[System 5]					
Radius	5.5167	6.0000	0.0000	0.0000	-0.4833	-0.4833
Arc E	[System 5]					
Radius	6.4097	6.0000	0.0000	0.0000	0.4097	0.4097
Arc F	[System 5]					
Radius	5.7360	6.0000	0.0000	0.0000	-0.2640	-0.2640
Distance H	[System 5]					
Distance Y	6.0475	6.0000	0.1000	-0.1000	0.0475	
Distance I	[System 5]					
Distance X	30.0345	30.0000	0.0000	0.0000	0.0345	0.0345
Distance J	[System 5]					
Distance X	30.2848	30.0000	0.0000	0.0000	0.2848	0.2848
Plane K	[System 5]					
Flatness	0.3164		0.0000			0.3164

Program: SLM tension samples.iwp Date: Wed Apr 10 2019 Time: 16:21:45
Units: mm, dec deg

Feature	Actual	Nominal	Upper	Lower	Dev/Nom	Out/Tol
Distance A	[System 5]					
Distance Y	10.0480	10.0000	0.0000	0.0000	0.0480	0.0480
Distance B	[System 5]					
Distance Y	10.0844	10.0000	0.0000	0.0000	0.0844	0.0844
Arc C	[System 5]					
Radius	5.6131	6.0000	0.0000	0.0000	-0.3869	-0.3869
Arc D	[System 5]					
Radius	5.8875	6.0000	0.0000	0.0000	-0.1125	-0.1125
Arc E	[System 5]					
Radius	5.8021	6.0000	0.0000	0.0000	-0.1979	-0.1979
Arc F	[System 5]					
Radius	6.0914	6.0000	0.0000	0.0000	0.0914	0.0914
Distance H	[System 5]					
Distance Y	6.0560	6.0000	0.1000	-0.1000	0.0560	
Distance I	[System 5]					
Distance X	30.0535	30.0000	0.0000	0.0000	0.0535	0.0535
Distance J	[System 5]					
Distance X	30.2533	30.0000	0.0000	0.0000	0.2533	0.2533
Plane K	[System 5]					
Flatness	0.2813		0.0000			0.2813

Program: SLM tension samples.iwp Date: Wed Apr 10 2019 Time: 16:27:07
Units: mm, dec deg

Feature	Actual	Nominal	Upper	Lower	Dev/Nom	Out/Tol
Distance A	[System 5]					
Distance Y	10.0523	10.0000	0.0000	0.0000	0.0523	0.0523
Distance B	[System 5]					
Distance Y	10.0268	10.0000	0.0000	0.0000	0.0268	0.0268
Arc C	[System 5]					
Radius	5.4332	6.0000	0.0000	0.0000	-0.5668	-0.5668
Arc D	[System 5]					
Radius	6.0151	6.0000	0.0000	0.0000	0.0151	0.0151
Arc E	[System 5]					
Radius	5.8137	6.0000	0.0000	0.0000	-0.1863	-0.1863
Arc F	[System 5]					
Radius	5.9781	6.0000	0.0000	0.0000	-0.0219	-0.0219
Distance H	[System 5]					
Distance Y	6.0493	6.0000	0.1000	-0.1000	0.0493	
Distance I	[System 5]					
Distance X	30.1126	30.0000	0.0000	0.0000	0.1126	0.1126
Distance J	[System 5]					
Distance X	30.2909	30.0000	0.0000	0.0000	0.2909	0.2909
Plane K	[System 5]					
Flatness	0.3062		0.0000			0.3062

Program: SLM tension samples.iwp Date: Wed Apr 10 2019 Time: 16:29:18
Units: mm, dec deg

Feature	Actual	Nominal	Upper	Lower	Dev/Nom	Out/Tol
Distance A	[System 5]					
Distance Y	10.0963	10.0000	0.0000	0.0000	0.0963	0.0963
Distance B	[System 5]					
Distance Y	10.1441	10.0000	0.0000	0.0000	0.1441	0.1441
Arc C	[System 5]					
Radius	6.5250	6.0000	0.0000	0.0000	0.5250	0.5250
Arc D	[System 5]					
Radius	6.0534	6.0000	0.0000	0.0000	0.0534	0.0534
Arc E	[System 5]					
Radius	5.9737	6.0000	0.0000	0.0000	-0.0263	-0.0263
Arc F	[System 5]					
Radius	5.4978	6.0000	0.0000	0.0000	-0.5022	-0.5022
Distance H	[System 5]					
Distance Y	6.0652	6.0000	0.1000	-0.1000	0.0652	
Distance I	[System 5]					
Distance X	30.0611	30.0000	0.0000	0.0000	0.0611	0.0611
Distance J	[System 5]					
Distance X	30.2818	30.0000	0.0000	0.0000	0.2818	0.2818
Plane K	[System 5]					
Flatness	0.2898		0.0000			0.2898

Program: SLM tension samples.iwp Date: Wed Apr 10 2019 Time: 16:31:21
Units: mm, dec deg

Feature	Actual	Nominal	Upper	Lower	Dev/Nom	Out/Tol
Distance A	[System 5]					
Distance Y	10.0452	10.0000	0.0000	0.0000	0.0452	0.0452
Distance B	[System 5]					
Distance Y	10.0457	10.0000	0.0000	0.0000	0.0457	0.0457
Arc C	[System 5]					
Radius	5.9695	6.0000	0.0000	0.0000	-0.0305	-0.0305
Arc D	[System 5]					
Radius	5.8754	6.0000	0.0000	0.0000	-0.1246	-0.1246
Arc E	[System 5]					
Radius	6.1871	6.0000	0.0000	0.0000	0.1871	0.1871
Arc F	[System 5]					
Radius	5.6783	6.0000	0.0000	0.0000	-0.3217	-0.3217
Distance G	[System 5]					
Distance X	31.7551	32.0000	0.0000	0.0000	-0.2449	-0.2449
Distance H	[System 5]					
Distance Y	6.0513	6.0000	0.1000	-0.1000	0.0513	
Distance I	[System 5]					
Distance X	30.0378	30.0000	0.0000	0.0000	0.0378	0.0378
Distance J	[System 5]					
Distance X	30.2920	30.0000	0.0000	0.0000	0.2920	0.2920
Plane K	[System 5]					
Flatness	0.2825		0.0000			0.2825

Program: SLM tension samples.iwp Date: Wed Apr 10 2019 Time: 16:34:08
Units: mm, dec deg

Feature	Actual	Nominal	Upper	Lower	Dev/Nom	Out/Tol
Distance A	[System 5]					
Distance Y	10.0693	10.0000	0.0000	0.0000	0.0693	0.0693
Distance B	[System 5]					
Distance Y	10.0535	10.0000	0.0000	0.0000	0.0535	0.0535
Arc C	[System 5]					
Radius	5.7126	6.0000	0.0000	0.0000	-0.2874	-0.2874
Arc D	[System 5]					
Radius	5.9482	6.0000	0.0000	0.0000	-0.0518	-0.0518
Arc E	[System 5]					
Radius	6.0317	6.0000	0.0000	0.0000	0.0317	0.0317
Arc F	[System 5]					
Radius	5.7843	6.0000	0.0000	0.0000	-0.2157	-0.2157
Distance H	[System 5]					
Distance Y	6.0608	6.0000	0.1000	-0.1000	0.0608	
Distance I	[System 5]					
Distance X	30.0863	30.0000	0.0000	0.0000	0.0863	0.0863
Distance J	[System 5]					
Distance X	30.2202	30.0000	0.0000	0.0000	0.2202	0.2202
Plane K	[System 5]					
Flatness	0.3066		0.0000			0.3066

Program: SLM tension samples.iwp Date: Wed Apr 10 2019 Time: 16:36:07
Units: mm, dec deg

Feature	Actual	Nominal	Upper	Lower	Dev/Nom	Out/Tol
Distance A	[System 5]					
Distance Y	10.1191	10.0000	0.0000	0.0000	0.1191	0.1191
Distance B	[System 5]					
Distance Y	10.1055	10.0000	0.0000	0.0000	0.1055	0.1055
Arc C	[System 5]					
Radius	5.4347	6.0000	0.0000	0.0000	-0.5653	-0.5653
Arc D	[System 5]					
Radius	5.9892	6.0000	0.0000	0.0000	-0.0108	-0.0108
Arc E	[System 5]					
Radius	5.9471	6.0000	0.0000	0.0000	-0.0529	-0.0529
Arc F	[System 5]					
Radius	6.1971	6.0000	0.0000	0.0000	0.1971	0.1971
Distance H	[System 5]					
Distance Y	6.1279	6.0000	0.1000	-0.1000	0.1279	0.0279
Distance I	[System 5]					
Distance X	30.1644	30.0000	0.0000	0.0000	0.1644	0.1644
Distance J	[System 5]					
Distance X	30.3294	30.0000	0.0000	0.0000	0.3294	0.3294
Plane K	[System 5]					
Flatness	0.2978		0.0000			0.2978

Program: SLM tension samples.iwp Date: Wed Apr 10 2019 Time: 16:39:03
Units: mm, dec deg

Feature	Actual	Nominal	Upper	Lower	Dev/Nom	Out/Tol
Distance A	[System 5]					
Distance Y	10.0533	10.0000	0.0000	0.0000	0.0533	0.0533
Distance B	[System 5]					
Distance Y	10.0766	10.0000	0.0000	0.0000	0.0766	0.0766
Arc C	[System 5]					
Radius	6.2623	6.0000	0.0000	0.0000	0.2623	0.2623
Arc D	[System 5]					
Radius	5.9309	6.0000	0.0000	0.0000	-0.0691	-0.0691
Arc E	[System 5]					
Radius	6.3994	6.0000	0.0000	0.0000	0.3994	0.3994
Arc F	[System 5]					
Radius	5.7160	6.0000	0.0000	0.0000	-0.2840	-0.2840
Distance H	[System 5]					
Distance Y	6.0677	6.0000	0.1000	-0.1000	0.0677	
Distance I	[System 5]					
Distance X	30.0605	30.0000	0.0000	0.0000	0.0605	0.0605
Distance J	[System 5]					
Distance X	30.3285	30.0000	0.0000	0.0000	0.3285	0.3285
Plane K	[System 5]					
Flatness	0.2755		0.0000			0.2755

Program: SLM tension samples.iwp Date: Wed Apr 10 2019 Time: 16:41:01
Units: mm, dec deg

Feature	Actual	Nominal	Upper	Lower	Dev/Nom	Out/Tol
Distance A	[System 5]					
Distance Y	10.0452	10.0000	0.0000	0.0000	0.0452	0.0452
Distance B	[System 5]					
Distance Y	10.0957	10.0000	0.0000	0.0000	0.0957	0.0957
Arc C	[System 5]					
Radius	5.7499	6.0000	0.0000	0.0000	-0.2501	-0.2501
Arc D	[System 5]					
Radius	5.7267	6.0000	0.0000	0.0000	-0.2733	-0.2733
Arc E	[System 5]					
Radius	5.7877	6.0000	0.0000	0.0000	-0.2123	-0.2123
Arc F	[System 5]					
Radius	5.5219	6.0000	0.0000	0.0000	-0.4781	-0.4781
Distance H	[System 5]					
Distance Y	6.0398	6.0000	0.1000	-0.1000	0.0398	
Distance I	[System 5]					
Distance X	30.0910	30.0000	0.0000	0.0000	0.0910	0.0910
Distance J	[System 5]					
Distance X	30.3493	30.0000	0.0000	0.0000	0.3493	0.3493
Plane K	[System 5]					
Flatness	0.2900		0.0000			0.2900

Program: SLM tension samples.iwp Date: Wed Apr 10 2019 Time: 16:42:48
Units: mm, dec deg

Feature	Actual	Nominal	Upper	Lower	Dev/Nom	Out/Tol
Distance A	[System 5]					
Distance Y	10.0804	10.0000	0.0000	0.0000	0.0804	0.0804
Distance B	[System 5]					
Distance Y	10.0888	10.0000	0.0000	0.0000	0.0888	0.0888
Arc C	[System 5]					
Radius	5.5606	6.0000	0.0000	0.0000	-0.4394	-0.4394
Arc D	[System 5]					
Radius	6.2472	6.0000	0.0000	0.0000	0.2472	0.2472
Arc E	[System 5]					
Radius	5.9522	6.0000	0.0000	0.0000	-0.0478	-0.0478
Arc F	[System 5]					
Radius	5.8057	6.0000	0.0000	0.0000	-0.1943	-0.1943
Distance H	[System 5]					
Distance Y	6.0775	6.0000	0.1000	-0.1000	0.0775	
Distance I	[System 5]					
Distance X	30.0800	30.0000	0.0000	0.0000	0.0800	0.0800
Distance J	[System 5]					
Distance X	30.2982	30.0000	0.0000	0.0000	0.2982	0.2982
Plane K	[System 5]					
Flatness	0.2768		0.0000			0.2768

Program: SLM tension samples.iwp Date: Wed Apr 10 2019 Time: 16:44:57
Units: mm, dec deg

Feature	Actual	Nominal	Upper	Lower	Dev/Nom	Out/Tol
Distance A	[System 5]					
Distance Y	10.0626	10.0000	0.0000	0.0000	0.0626	0.0626
Distance B	[System 5]					
Distance Y	10.0809	10.0000	0.0000	0.0000	0.0809	0.0809
Arc C	[System 5]					
Radius	6.2199	6.0000	0.0000	0.0000	0.2199	0.2199
Arc D	[System 5]					
Radius	5.7203	6.0000	0.0000	0.0000	-0.2797	-0.2797
Arc E	[System 5]					
Radius	5.4445	6.0000	0.0000	0.0000	-0.5555	-0.5555
Arc F	[System 5]					
Radius	5.7508	6.0000	0.0000	0.0000	-0.2492	-0.2492
Distance H	[System 5]					
Distance Y	6.0657	6.0000	0.1000	-0.1000	0.0657	
Distance I	[System 5]					
Distance X	30.0708	30.0000	0.0000	0.0000	0.0708	0.0708
Distance J	[System 5]					
Distance X	30.3256	30.0000	0.0000	0.0000	0.3256	0.3256
Plane K	[System 5]					
Flatness	0.2588		0.0000			0.2588

Program: SLM tension samples SIDE.iwp Date: Wed Apr 10 2019 Time: 16:47:55
Units: mm, dec deg

Feature	Actual	Nominal	Upper	Lower	Dev/Nom	Out/Tol
Distance L	[System 10]					
Distance XY	6.0634	6.0000	0.0000	0.0000	0.0634	0.0634

Program: SLM tension samples SIDE.iwp Date: Wed Apr 10 2019 Time: 16:49:15
Units: mm, dec deg

Feature	Actual	Nominal	Upper	Lower	Dev/Nom	Out/Tol
Distance L	[System 10]					
Distance XY	6.0685	6.0000	0.0000	0.0000	0.0685	0.0685

Program: SLM tension samples SIDE.iwp Date: Wed Apr 10 2019 Time: 16:50:48
Units: mm, dec deg

Feature	Actual	Nominal	Upper	Lower	Dev/Nom	Out/Tol
Distance L	[System 10]					
Distance XY	6.0355	6.0000	0.0000	0.0000	0.0355	0.0355

Program: SLM tension samples SIDE.iwp Date: Wed Apr 10 2019 Time: 16:53:38
Units: mm, dec deg

Feature	Actual	Nominal	Upper	Lower	Dev/Nom	Out/Tol
Distance L	[System 10]					
Distance XY	6.0253	6.0000	0.0000	0.0000	0.0253	0.0253

Program: SLM tension samples SIDE.iwp Date: Wed Apr 10 2019 Time: 16:54:49
Units: mm, dec deg

Feature	Actual	Nominal	Upper	Lower	Dev/Nom	Out/Tol
Distance L	[System 10]					
Distance XY	6.0193	6.0000	0.0000	0.0000	0.0193	0.0193

Program: SLM tension samples SIDE.iwp Date: Wed Apr 10 2019 Time: 16:55:59
Units: mm, dec deg

Feature	Actual	Nominal	Upper	Lower	Dev/Nom	Out/Tol
Distance L	[System 10]					
Distance XY	6.0210	6.0000	0.0000	0.0000	0.0210	0.0210

Program: SLM tension samples SIDE.iwp Date: Wed Apr 10 2019 Time: 16:57:12
Units: mm, dec deg

Feature	Actual	Nominal	Upper	Lower	Dev/Nom	Out/Tol
Distance L	[System 10]					
Distance XY	6.0259	6.0000	0.0000	0.0000	0.0259	0.0259

Program: SLM tension samples SIDE.iwp Date: Wed Apr 10 2019 Time: 16:58:31
Units: mm, dec deg

Feature	Actual	Nominal	Upper	Lower	Dev/Nom	Out/Tol
Distance L	[System 10]					
Distance XY	6.0403	6.0000	0.0000	0.0000	0.0403	0.0403

Program: SLM tension samples SIDE.iwp Date: Wed Apr 10 2019 Time: 16:59:47
Units: mm, dec deg

Feature	Actual	Nominal	Upper	Lower	Dev/Nom	Out/Tol
Distance L	[System 10]					
Distance XY	6.0078	6.0000	0.0000	0.0000	0.0078	0.0078

Program: SLM tension samples SIDE.iwp Date: Wed Apr 10 2019 Time: 17:02:31
Units: mm, dec deg

Feature	Actual	Nominal	Upper	Lower	Dev/Nom	Out/Tol
Distance L	[System 10]					
Distance XY	6.0416	6.0000	0.0000	0.0000	0.0416	0.0416

Program: SLM tension samples SIDE.iwp Date: Wed Apr 10 2019 Time: 17:03:40
Units: mm, dec deg

Feature	Actual	Nominal	Upper	Lower	Dev/Nom	Out/Tol
Distance L	[System 10]					
Distance XY	6.0300	6.0000	0.0000	0.0000	0.0300	0.0300

Program: SLM tension samples SIDE.iwp Date: Wed Apr 10 2019 Time: 17:05:03
Units: mm, dec deg

Feature	Actual	Nominal	Upper	Lower	Dev/Nom	Out/Tol
Distance L	[System 10]					
Distance XY	6.0401	6.0000	0.0000	0.0000	0.0401	0.0401

Program: SLM tension samples SIDE.iwp Date: Wed Apr 10 2019 Time: 17:06:25
Units: mm, dec deg

Feature	Actual	Nominal	Upper	Lower	Dev/Nom	Out/Tol
Distance L	[System 10]					
Distance XY	6.0338	6.0000	0.0000	0.0000	0.0338	0.0338

Program: SLM tension samples SIDE.iwp Date: Wed Apr 10 2019 Time: 17:07:42
Units: mm, dec deg

Feature	Actual	Nominal	Upper	Lower	Dev/Nom	Out/Tol
Distance L	[System 10]					
Distance XY	6.0660	6.0000	0.0000	0.0000	0.0660	0.0660

Program: SLM tension samples SIDE.iwp Date: Wed Apr 10 2019 Time: 17:08:58
Units: mm, dec deg

Feature	Actual	Nominal	Upper	Lower	Dev/Nom	Out/Tol
Distance L	[System 10]					
Distance XY	6.0330	6.0000	0.0000	0.0000	0.0330	0.0330

Program: DIST G.iwp
Units: mm, dec deg

Date: Tue Apr 16 2019 Time: 13:41:57

Feature	Actual	Nominal	Upper	Lower	Dev/Nom	Out/Tol
Distance G	[System 5]					
Distance X	32.0588	32.0000	0.0000	0.0000	0.0588	0.0588
Distance G2	[System 5]					
Distance X	32.0804	32.0000	0.0000	0.0000	0.0804	0.0804

Program: DIST G.iwp
Units: mm, dec deg

Date: Tue Apr 16 2019 Time: 13:49:30

Feature	Actual	Nominal	Upper	Lower	Dev/Nom	Out/Tol
Distance G2	[System 5]					
Distance X	31.7699	32.0000	0.0000	0.0000	-0.2301	-0.2301

Program: DIST G.iwp
Units: mm, dec deg

Date: Tue Apr 16 2019 Time: 13:51:04

Feature	Actual	Nominal	Upper	Lower	Dev/Nom	Out/Tol
Distance G2	[System 5]					
Distance X	31.7693	32.0000	0.0000	0.0000	-0.2307	-0.2307

Program: DIST G.iwp
Units: mm, dec deg

Date: Tue Apr 16 2019 Time: 13:53:34

Feature	Actual	Nominal	Upper	Lower	Dev/Nom	Out/Tol
Distance G2	[System 5]					
Distance X	31.9746	32.0000	0.0000	0.0000	-0.0254	-0.0254

Program: DIST G.iwp
Units: mm, dec deg

Date: Tue Apr 16 2019 Time: 14:02:26

Feature	Actual	Nominal	Upper	Lower	Dev/Nom	Out/Tol
Distance G	[System 5]					
Distance X	31.9691	32.0000	0.0000	0.0000	-0.0309	-0.0309
Distance G2	[System 5]					
Distance X	31.9862	32.0000	0.0000	0.0000	-0.0138	-0.0138

Program: DIST G.iwp
Units: mm, dec deg

Date: Tue Apr 16 2019 Time: 14:05:21

Feature	Actual	Nominal	Upper	Lower	Dev/Nom	Out/Tol
Distance G2	[System 5]					
Distance X	31.8404	32.0000	0.0000	0.0000	-0.1596	-0.1596

Program: DIST G.iwp
Units: mm, dec deg

Date: Tue Apr 16 2019 Time: 14:07:34

Feature	Actual	Nominal	Upper	Lower	Dev/Nom	Out/Tol
Distance G2	[System 5]					
Distance X	31.7188	32.0000	0.0000	0.0000	-0.2812	-0.2812

Program: DIST G.iwp
Units: mm, dec deg

Date: Tue Apr 16 2019 Time: 14:09:01

Feature	Actual	Nominal	Upper	Lower	Dev/Nom	Out/Tol
Distance G	[System 5]					
Distance X	31.7391	32.0000	0.0000	0.0000	-0.2609	-0.2609
Distance G2	[System 5]					
Distance X	31.7753	32.0000	0.0000	0.0000	-0.2247	-0.2247

Program: DIST G.iwp
Units: mm, dec deg

Date: Tue Apr 16 2019 Time: 14:10:09

Feature	Actual	Nominal	Upper	Lower	Dev/Nom	Out/Tol
Distance G2	[System 5]					
Distance X	32.0913	32.0000	0.0000	0.0000	0.0913	0.0913

Program: DIST G.iwp
Units: mm, dec deg

Date: Tue Apr 16 2019 Time: 14:11:53

Feature	Actual	Nominal	Upper	Lower	Dev/Nom	Out/Tol
Distance G2	[System 5]					
Distance X	32.1005	32.0000	0.0000	0.0000	0.1005	0.1005

Program: DIST G.iwp
Units: mm, dec deg

Date: Tue Apr 16 2019 Time: 14:14:06

Feature	Actual	Nominal	Upper	Lower	Dev/Nom	Out/Tol
Distance G2	[System 5]					
Distance X	31.9067	32.0000	0.0000	0.0000	-0.0933	-0.0933

Program: DIST G.iwp
Units: mm, dec deg

Date: Tue Apr 16 2019 Time: 14:17:04

Feature	Actual	Nominal	Upper	Lower	Dev/Nom	Out/Tol
Distance G	[System 5]					
Distance X	31.7295	32.0000	0.0000	0.0000	-0.2705	-0.2705
Distance G2	[System 5]					
Distance X	31.9835	32.0000	0.0000	0.0000	-0.0165	-0.0165

Program: DIST G.iwp
Units: mm, dec deg

Date: Tue Apr 16 2019 Time: 14:19:33

Feature	Actual	Nominal	Upper	Lower	Dev/Nom	Out/Tol
Distance G2	[System 5]					
Distance X	31.7804	32.0000	0.0000	0.0000	-0.2196	-0.2196

Program: DIST G.iwp
Units: mm, dec deg

Date: Tue Apr 16 2019 Time: 14:26:22

Feature	Actual	Nominal	Upper	Lower	Dev/Nom	Out/Tol
Distance G2	[System 5]					
Distance X	31.3729	32.0000	0.0000	0.0000	-0.6271	-0.6271

Program: DIST G.iwp
Units: mm, dec deg

Date: Tue Apr 16 2019 Time: 14:28:45

Feature	Actual	Nominal	Upper	Lower	Dev/Nom	Out/Tol
Distance G	[System 5]					
Distance X	31.9170	32.0000	0.0000	0.0000	-0.0830	-0.0830
Distance G2	[System 5]					
Distance X	31.8878	32.0000	0.0000	0.0000	-0.1122	-0.1122

Appendix C: Full Location Influence Testing Results

Results Table 1

	Specimen Label	Young's Modulus (GPa)	Yield Stress (Offset 0.2%) (MPa)	Tensile Stress (Max) (MPa)	Elongation (%)
1	190315_0104-Brown-I	180.59	470.87	596.05	14.69
2	190315_0104-Brown-II	175.21	465.43	603.74	43.22
3	190315_0104-Brown-III	160.48	470.81	580.82	8.46
4	190315_0104-Brown-IV	182.32	474.03	567.93	4.87
5	190315_0104-Brown-V	155.75	464.53	601.41	32.76
6	190315_0104-Black-I	185.12	467.89	479.29	1.28
7	190315_0104-Black-II	176.67	473.94	594.58	12.36
8	190315_0104-Black-III	159.83	474.61	590.82	10.97
9	190315_0104-Black-IV	155.97	474.99	605.5	37.49
10	190315_0104-Black-V	158.49	478.36	606.35	43.67
11	190315_0104-Purple-I	179.63	473.94	588.39	9.09
12	190315_0104-Purple-II	174.81	474.6	598.02	14.5
13	190315_0104-Purple-III	160.48	485.78	609.41	43.34
14	190315_0104-Purple-IV	183.1	481.37	604.31	22.56
15	190315_0104-Purple-V	177.37	483.74	607.22	42.17